Journal of Volcanology and Geothermal Research 425 (2022) 107518

Contents lists available at ScienceDirect

Journal of Volcanology and Geothermal Research

journal homepage: www.journals.elsevier.com/journal-of-volcanology-and-geothermal-research

Invited review article

A review of tectonic, elastic and visco-elastic models exploring the deformation patterns throughout the eruption of Soufrière Hills volcano on Montserrat, West Indies

J.W. Neuberg [a,*], B. Taisne [b], M. Burton [c], G.A. Ryan [d,e], E. Calder [f], N. Fournier [g], A.S.D. Collinson [a]

[a] School of Earth and Environment, Leeds University, UK
[b] Earth Observatory of Singapore, Nanyang Technological University, Singapore
[c] Department of Earth & Environmental Sciences, Manchester University, UK
[d] Montserrat Volcano Observatory, Flemmings, Montserrat, West Indies
[e] Seismic Research Centre, University of West Indies, Saint Augustine, Trinidad and Tobago
[f] School of GeoSciences, University of Edinburgh, UK
[g] GNS Science, New Zealand

ARTICLE INFO

Keywords:
Soufrière Hills
GPS
Deformation
Magma compressibility
Maxwell rheology
Visco-elastic response

ABSTRACT

Since the eruption began in 1995, Soufrière Hills volcano on Montserrat has been characterised by five phases of magma extrusion and corresponding pauses. Despite a lack of eruptive surface activity since 2010, the volcano continues to show signs of unrest in the form of ongoing outgassing, and inflation of the entire island of Montserrat. Using numerical modelling, we compare a set of contrasting deformation models in an attempt to understand the current state of Soufrière Hills volcano, and to gauge its future eruption potential. We apply a suite of deformation models including faults and dykes, and an ellipsoidal source geometry to all phases and pauses covering the entire eruptive history from 1995 through 2020. Based on recent petrological evidence suggesting no recent injection of magma from depth after an initial magma intrusion, we test the hypothesis that the ongoing inflation of Montserrat could be explained by a visco-elastic, crustal response to the initial magma intrusion without a renewed pressurisation due to magma injection. In contrast to previous modelling attempts, we focus on conceptual models and compare elastic- with several visco-elastic models taking temperature-dependent viscosity models, tectonic components, mass balance, magma compressibility and outgassing data into account. We explore a wide parameter space in a Generalised Maxwell Rheology to explain the observed deformation patterns, and demonstrate that a realistic, depth-dependent distribution of visco-elastic parameters does not allow an interpretation of the deformation signal without any magma influx or further pressurisation. Within the range of large uncertainties attached to the visco-elastic model parameters we show that visco-elasticity reduces the degree of ongoing pressurisation or magma influx into a crustal reservoir by a few percent. We conclude that magma influx at a rate of 0.10 to 0.57 m^3/s is the most likely explanation of the current deformation pattern and is also in agreement with mass balance considerations and current SO_2 flux observations.

1. Introduction

The current eruption of Soufrière Hills volcano (SHV), Montserrat (Fig. 1), began in 1995, and has been well documented in the literature (e.g. Kokelaar, 2002; Wadge et al., 2014). The eruption has been characterised by five episodes of lava dome growth punctuated by dome collapses, Vulcanian explosions, outgassing and ash venting (e.g. Edmonds et al., 2001, 2002; Watts et al., 2002; Hautmann et al., 2014). As depicted in Fig. 2, pauses of differing duration have separated each phase such that despite lasting more than 25 years, the volcano was only actively extruding for a total of 8.5 years (Wadge et al., 2014). The last extrusive event recorded at the volcano on 11 February 2010, coincided

* Corresponding author.
E-mail address: J.Neuberg@leeds.ac.uk (J.W. Neuberg).

https://doi.org/10.1016/j.jvolgeores.2022.107518
Received 30 August 2021; Received in revised form 1 March 2022; Accepted 3 March 2022
Available online 11 March 2022

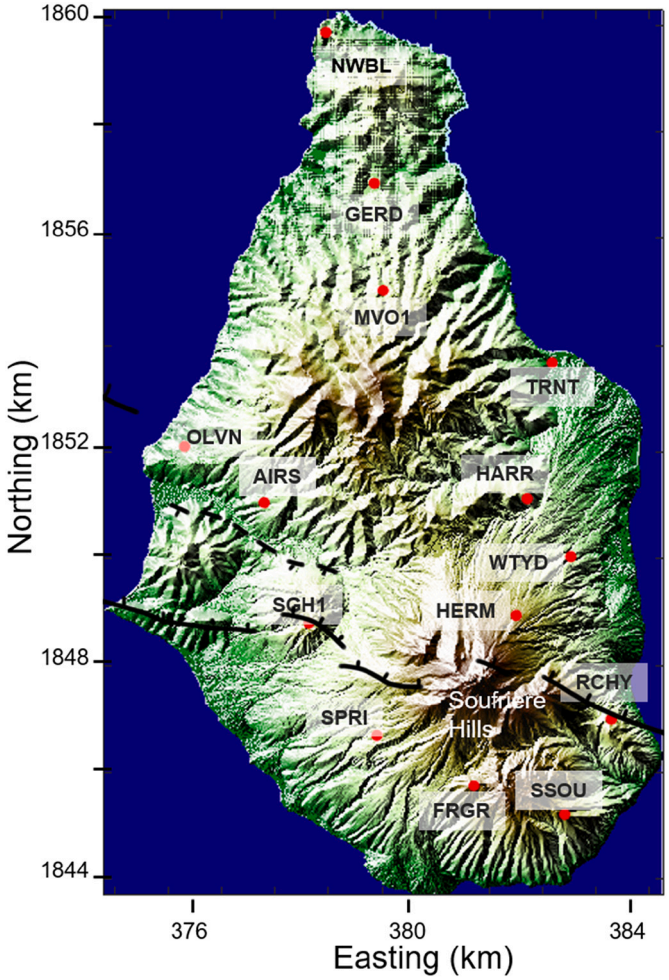

Fig. 1. Active Soufrière Hills volcano in the south of Montserrat; locations of major faults (Feuillet et al., 2010) and cGPS stations used in this study.

with the partial collapse of the northern section of the dome (Stinton et al., 2014). Since this event, the volcano has entered a period of apparent quiescence with an average of 1.2 seismic events per day (Stinton et al., 2014). By January 2022, Pause 5 has lasted for 12 years, significantly longer than any other pause, the immediate implication being that it is a pause - not the end of the eruption. A mean daily SO_2 flux of approximately 200 t/day (Stinton et al., 2020), recorded until April 2020, and ongoing inflation of the island, continuously monitored by cGPS (Fig. 2), are indications of ongoing volcanic unrest. Due to the lack of a monitoring baseline for the background activity of Soufrière Hills, the question remains as to whether these signals indicate potential future extrusive activity, or if the eruption can finally be declared over.

Throughout the history of the eruption, there have been many attempts to determine the configuration of the SHV plumbing system summarised in Elsworth et al. (2014). Deformation models fall into two broad categories - either vertically-stacked magma reservoirs (Elsworth et al., 2008, 2014; Foroozan et al., 2010, 2011; Hautmann et al., 2010) or single, vertically-extended sources (Voight et al., 2010). The source geometries range from spheres to prolate or oblate ellipsoids with rotational symmetry, which results for some studies in the necessity for partial or complete omission of certain GPS stations in order to match model output and GPS data (e.g. Hautmann et al., 2010; Foroozan et al., 2011).

In contrast to attempting a detailed, perfect match of deformation data recorded on all stations of the continuous GPS network (cGPS), we employ an entire suite of contrasting, numerical models and focus on their conceptual differences. We aim at answering the critical question whether the eruption is continuing or not. We follow the conceptual models that have been guiding the discussions of the Scientific Advisory Committee on Montserrat Volcanic Activity throughout the eruption. These models range from magma extrusion and reservoir refill, to the influence of tectonic effects, potential contributions of crystallisation to the pressurisation of the system, to the final end-member model of a visco-elastic response to a major intrusion that has actually ceased several years ago.

We start with a purely elastic model to determine the source geometry of a deformation source which can match the deformation data for Pause 5. In order to explore processes alternative to magma influx explaining the ongoing inflation during Pause 5, we also address the potential contributions of local tectonics such as the WNW- trending

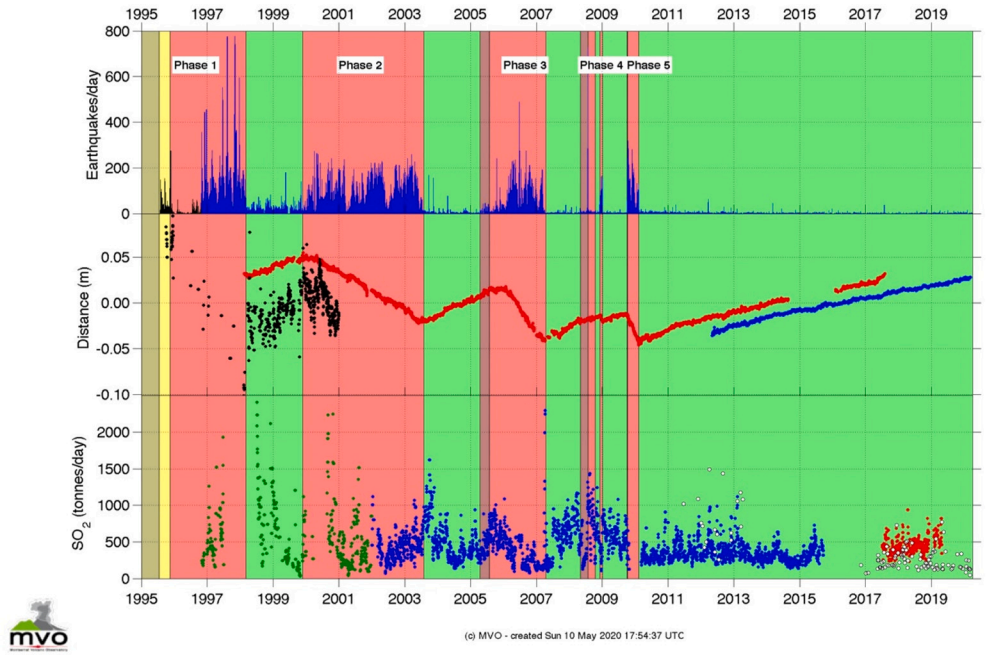

Fig. 2. Monitoring data for the entire duration of the ongoing eruption at Soufrière Hills volcano with the number of seismic events per day (top), vertical displacement for HARR (black) and radial ground motion of MVO1 (red) and NWBL (blue) relative to the dome centre (middle). SO_2 daily flux (bottom) monitored with different methods: COSPEC (green), scanning DOAS (blue /red), traverse DOAS (white). Despite its prolonged duration, Pause 5 is characterised by ongoing SO_2 outgassing and surface deformation, but limited seismicity. Adopted from Stinton et al. (2020).

Belham Valley fault, part of the Montserrat-Bouillante fault system (Feuillet et al., 2010) which is related to the wider regional tectonics of the Northern Lesser Antilles section of the Caribbean plate with a North-South extension (Wadge et al., 2014). We then adopt the geometry of a central, elliptical source to model the dominant patterns of all eruptive phases and pauses, as well as its anisotropic nature. By considering magma compressibility and extruded volume, we estimate the respective volume changes for all phases and pauses throughout the eruption. In this step, we interpret the iconic saw-tooth pattern in the deformation data (Fig. 1) as erupted and re-charged material, respectively. Given recent petrological evidence (McGee et al., 2019) which suggested that the intrusion of mafic magma had ceased by 2004, we employ a set of visco-elastic models based on a temperature-dependent Maxwell rheology, and test the alternative hypothesis that the observed saw-tooth deformation pattern can be explained without any further magma influx.

2. Continuous GPS data

The cGPS network on Montserrat comprises 14 stations distributed across the island (Fig. 1). The data used for our initial analysis of Pause 5 covered a time period of 3 years from August 2012 – July 2015, which presents a sufficiently long time interval after the previous eruptive activity of February 2010, and a short ash-venting episode that occurred in March 2012, in order to focus on the underlying deformation trend. The velocity of each station has been calculated relative to the motion of the Caribbean Plate using the GAMIT/GLOBK tool suite (Herring et al., 2010a, 2010b). The plate motion has been defined by a number of stations and the averaged displacements for the 2012–2015 period were derived from these velocities.

Due to the short durations of Phases 4, 5 and Pause 4, and the requirement for a data coverage of at least one-year for a sufficiently accurate deformation estimate, we omit these stages from the following comparison depicted in Fig. 3. When normalised relative to the station HARR, which is a station with data available for the entire eruptive history, there is a remarkable similarity in relative magnitude of the horizontal, and, to a lesser extent, of the vertical velocities across the stations for all stages of the eruption. The relative horizontal magnitudes are the same, both for the eruptive phases and pauses. With the vertical displacements being inherently noisier than the horizontal components, we assume that the displacement rate can be caused by the same source geometry throughout the eruption since it began in 1995. Furthermore, this highlights the repetitiveness of the source process, for both apparent inflation and deflation, affecting all but the closest stations with the only difference being the overall magnitude of displacement rate.

In agreement with the other pauses (e.g. Hautmann et al., 2010; Voight et al., 2010; Foroozan et al., 2011), the majority of the cGPS stations showed a displacement away from the volcano that increases with distance (Figs. 4 and 5). We assume the region to the south of the volcano would show a similar displacement pattern to that in the north,

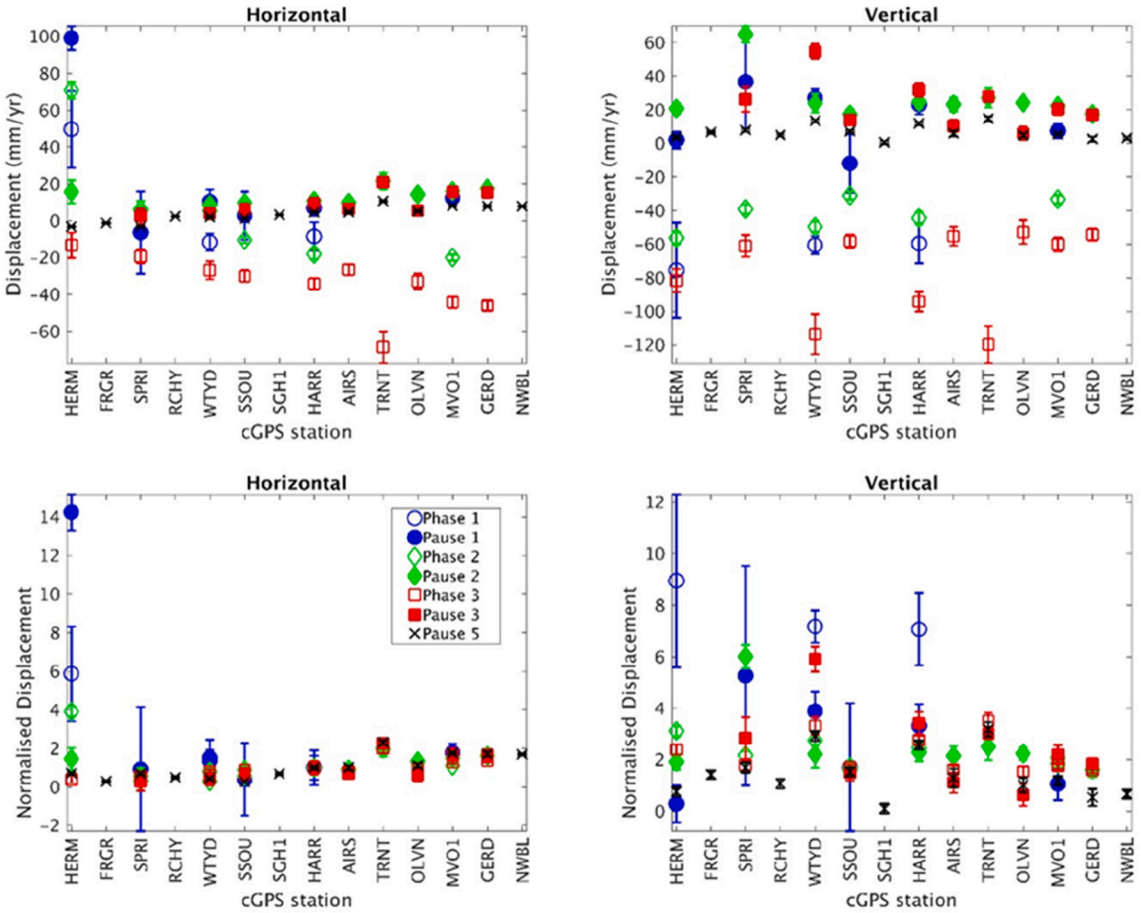

Fig. 3. Horizontal and vertical displacement rates for Phases (1–3) and Pauses (1–3, 5) (top) in order of increasing distance from the volcanic edifice. All data are normalised relative to the horizontal displacement at HARR (bottom). A negative horizontal displacement represents motion towards the volcano. Therefore, the displacement direction is generally towards the volcano during phases and away from it during pauses. For the normalised horizontal cGPS data, all stations except HERM are in good agreement indicating an identical source geometry throughout the eruption. The discrepancy with HERM may be due to the proximity to the volcano, and a greater sensitivity to shallow conduit/dome processes. Phase 1 – Pause 3 data adapted from Mattioli et al. (2010) and Foroozan et al. (2011). No data plotted for Phase 4–5 due to their limited duration.

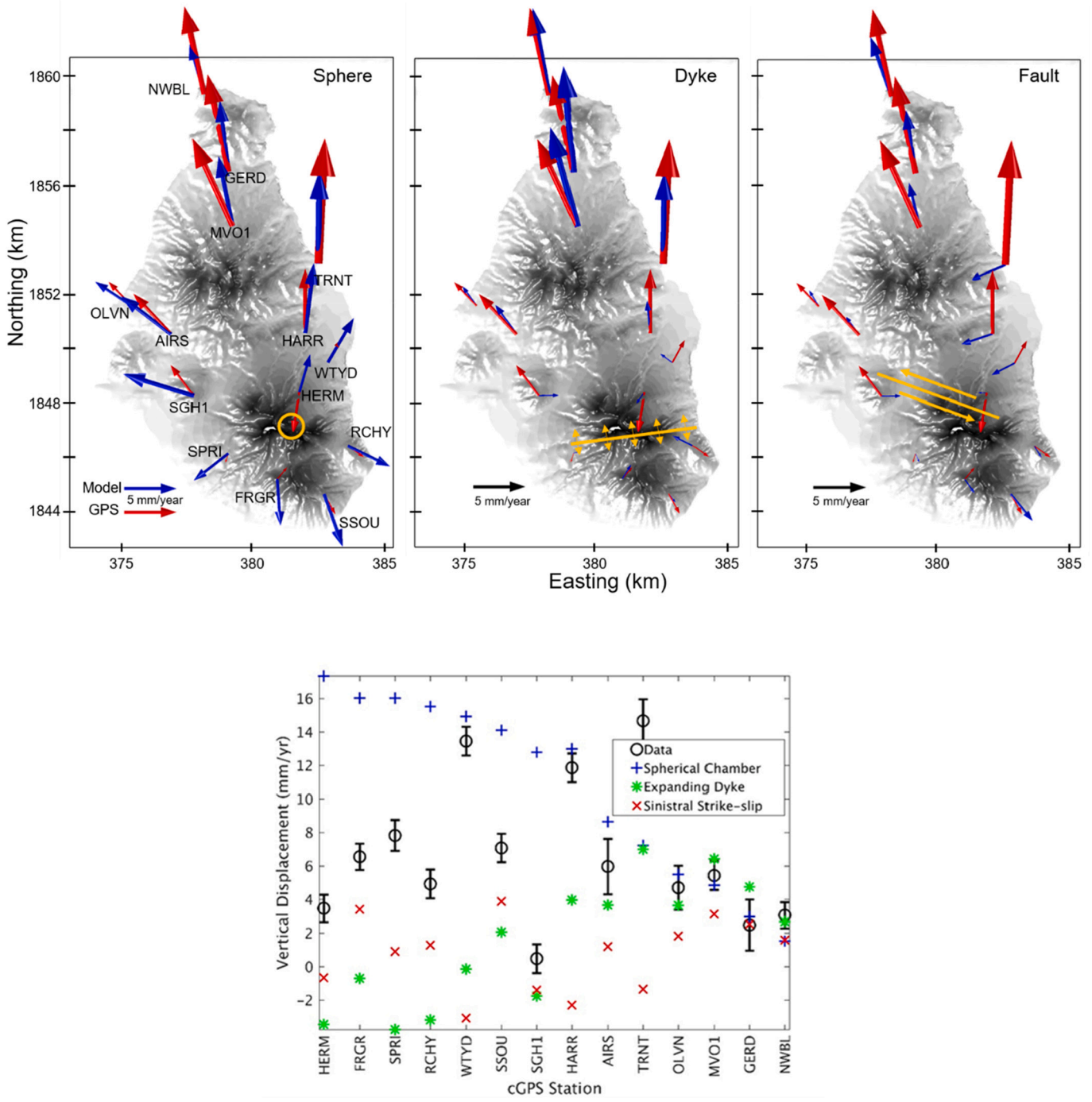

Fig. 4. Horizontal (top) and vertical displacement rates (bottom) for basic source models, fitting spherical reservoir, dyke and sinistral strike-slip. The stations are listed in order of increasing horizontal distance from the volcano. High resolution topography is included and the location and orientation of the sources are marked on the maps. For both the horizontal and vertical component of the displacement, the expanding dyke (I_D) shows the closest match to the Pause 5 data.

but due to the limited size of the island, and the location of the volcano in the south, this can be neither corroborated nor invalidated. The three closest cGPS stations to the volcano (HERM, SPRI and FRGR) deviate from this pattern by recording motion towards it. This is different to the other pauses in the eruption history and may indicate a deviation of some processes affecting these proximal stations which will be further discussed below.

The characteristic deformation patterns that guide our modelling approach are the increasing deflation rates for consecutive phases, in contrast to the decreasing inflation rates for pauses, and the sharp transitions between pauses and phases as depicted in Fig. 2.

3. Numerical modelling

To determine the configuration of sources required to replicate the current displacement pattern on Montserrat, we have created a set of numerical models using Comsol Multiphysics 5.4, which utilises a finite element method. Simple models have been calibrated against analytical solutions (e.g. Mogi, 1958; Okada, 1985, 1992; McTigue, 1987; Del Negro et al., 2009), and have been used to assess the potential contribution of several source types such as a tectonic (strike-slip) versus a volume source (dyke or spherical chamber). Because the study area is small (< 10 km) compared to its distance to the subduction zone (> 200

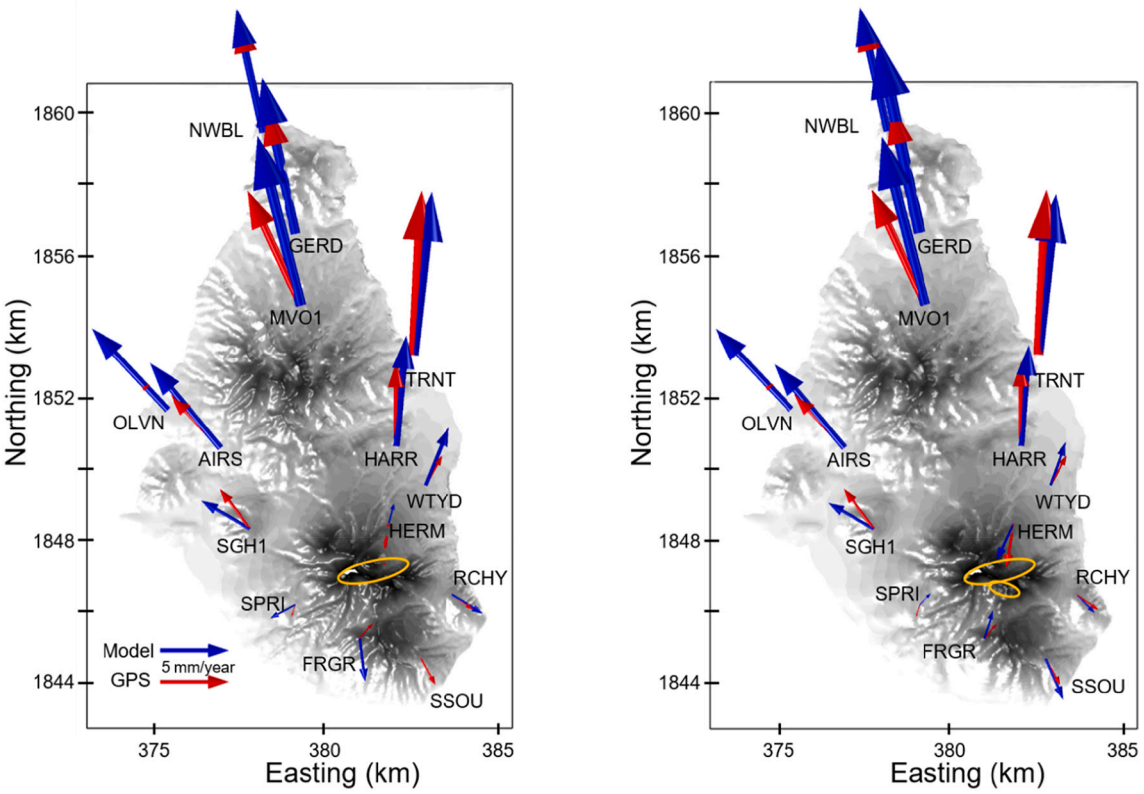

Fig. 5. Horizontal displacement rates (blue) for the 'Initial Elastic Models' E_{1E} and E_{2E} compared to the Pause 5 data (red). Source geometry (yellow) is projected onto the surface. Left: only deep source is modelled E_{1E}. Right: dual source of deep and shallow ellipsoids are used E_{2E} (see text). Note, the shallow source affects only the stations HERM, SPRI and FRGR close to the volcano.

km), vertical displacements due to vertical plate motion would be similar (i.e., within the uncertainty on daily positions) at all stations in Montserrat. We therefore assume that observed vertical deformation variations across the network are caused by local, plate-internal tectonics or magmatic sources. We have systematically modified the location, size and orientation of each source type to achieve the optimum match to the data. Finally, once the source type has been established, source parameters have been further refined to optimise the match to the data.

The model geometry has been created with a central block with dimensions of 12 km × 18 km × 50 km, embedded in a larger block of lateral extent 300 km × 300 km and depth 50 km. Into this framework, we have inserted a variety of different source types and configurations. Volume sources have been modelled using spherical or elliptical geometries whereas tectonic fault movements have been modelled as finite planar surfaces. For spherical and elliptical magmatic sources, we have imposed pressure as boundary conditions; for dykes and faults we have employed displacement. We have modelled the elastic crust as either homogeneous with a Young's modulus of 10 GPa (e.g. Elsworth et al., 2014) and a Poisson's ratio of 0.25, or later in Section 5.4, have employed a depth-dependent model based on seismic tomography (Paulatto, 2011; Paulatto et al., 2019) where correction factors of 0.67 to 0.11 have been applied to account for the difference in elastic behaviour between short-period seismic time scales and long-period, static deformation (Gudmundsson, 1990). For the visco-elastic models we have used the same source geometry and average viscosities in the range between 10^{18} and 10^{19} Pas, and later temperature/depth-dependent viscosity distributions derived from different temperature models according to the Arrhenius approximation. We used roller boundary conditions at the sides, fixed conditions at the bottom, and a free surface at the top. The finite element mesh comprising tetrahedral elements of varying sizes consists of up to 100,000 elements resulting in 4 million degrees of freedom.

4. Modelling results

Initially, our modelling attempts have focussed on data from Pause 5, which has the best data coverage and shows the most consistent long-term trend. After finding the model geometry that best matches the data set, we have applied the same source type to previous eruptive phases and pauses.

4.1. Effect of topography

Previous studies have often assumed a flat surface to their models, stating topography has little effect on the surface displacement pattern for deep sources (e.g. Hautmann et al., 2010). Marsden et al. (2019) have demonstrated that, to some extent, this is true for isotropic sources, but it is not applicable for more complex sources. They found a significant difference close to the volcanic edifice, where high dome topography affects both the magnitude of surface displacement and its direction, which may be completely reversed (Marsden et al., 2019). However, regarding the main objective of this study, the influence of topography does not play an important role to find the principle causes behind the ongoing, island-wide inflation.

4.2. Basic source models: Dyke, fault and their combination

Our overall modelling strategy is led by the aim to explore source models alternative to previous studies that were based on pressurising deep magma reservoirs. There is significant evidence for previous tectonic activity in the vicinity of the island, in particular the presence of faults crossing the island, including the Montserrat-Havers Fault, the Belham valley Fault and the Richmond Hill Fault (Fig. 1) contributing to

the Montserrat-Bouillante Fault System (Feuillet et al., 2010). A regional GPS study by Lopez et al. (2006) indicates a small N-S intraplate extension in the area of the Lesser Antilles where Montserrat lies. The NNW trans-tensional fault system between Montserrat and Guadeloupe is thought to accommodate some of this extension. We approximate this tectonic extension as a NW-SE extension of the exterior northern and southern model boundaries. For example, a NW-SE extension of 10 mm/year at 25 km distance from the Belham Valley, in each direction, would result in an on-island extension of 2.5 mm/year.

Hence, the first set of models comprises strike-slip faults and expanding dykes (Fig. 4) which are employed individually with a simple sphere for comparison. For each source type, the depth of the top has been varied at 0.5 km intervals between 1 and 10 km below sea level (b.s.l.), for different vertical and horizontal extents, lateral positions and strike directions.

Fig. 4 shows best-fit results for each of the three basic source models. The spherical magma chamber (Model I_S) has an initial radius of 1 km, centred at 6 km b.s.l. and has been modelled with a pressure of 4 MPa resulting in a uniform radius increase by 0.25 m. The initial dyke (Model I_D) and strike-slip (Model I_F) sources both have dimensions of 5 km × 1 km × 1 m to which we have applied displacement boundary conditions of 0.5 m in each direction. The dyke depicted in Fig. 4 has been modelled with an orientation of 263° whilst the sinistral strike-slip motion has been simulated with a fault striking at 293°.

The results of the simple strike-slip sources show a bad match to the data, and using a WNW-trending orientation, parallel to the Belham Valley (Wadge et al., 2014), they only match the stations furthest north. In contrast, the expanding spherical and dyke sources both show a better match. However, unlike the spherical source model, an expanding dyke source (I_D) satisfies both, the non-rotationally symmetric nature of the data, as well as the requirement for an increased horizontal displacement with distance from the volcano. Due to the observed surface displacement pattern, characterised by increased horizontal displacement away from the volcano and a north-south trend, we discount rotationally symmetric sources, or their combinations, and sources located at less than 4 km depth. The mismatch with the GPS data in Fig. 4 is evident and results in an absolute data misfit of 28.1 mm for the dyke model I_D, 53.5 mm for the fault model I_F, and 43.2 mm for the spherical model I_S. Hence, we conclude that none of these three source types (I_S, I_D, and I_F) match the deformation data of Pause 5.

4.3. Initial volume models

After disregarding the basic source models (IS, ID, and IF) in the

Table 1
Summary of numerical models employed throughout this study.

Model Reference	Topography	Crustal Response	Description Source	Parameter Final/Range	Stations used
I_S	y	elastic	Expanding sphere	radius 1 [0.5, 2] km depth 6 [1,10] km expansion 0.25 m	all cGPS
I_D	y	elastic	Expanding dyke	dimension 5 × 1 km expansion 1 m azimuth 263° [200°,300°]	all
I_F	y	elastic	Sinistral fault	dimension 5 × 1 km strike-slip 1 m azimuth 293° [280°,300°]	all
E_{1E}	y	elastic	Expanding ellipsoid	0.6 × 0.6 × 2.0 km depth 6 [1, 10] km azimuth 263°	all
E_{2E}	y	elastic	Two expanding/ contracting ellipsoids	0.6 × 0.6 × 2.0 km depth 6 [1, 10] km azimuth 263° 0.3 × 0.3 × 1.0 km depth 0 [0,3] km azimuth 293°	all
E_{2Ex}	y	elastic	Two expanding/contracting ellipsoids with depth extension	0.6 × 0.6 × 2.0 km depth 6 [1, 10] km azimuth 263° 0.3 × 0.3 × 1.0 km depth 0 [0, 3] km azimuth 293° depth extension 8 [0,20] km pressure (10, 2.5] MPa/year	all
E_{1Ex}	y	elastic	Expanding single ellipsoid with depth extension	0.6 × 0.6 × 2.0 km depth 6 [1, 10] km azimuth 263° depth extension 8 [0, 20] km pressure [10,2.5] MPa/year	all
V_H	n	visco-elastic Maxwell homogeneous	Expanding single ellipsoid with depth extension	source as above viscosity [1.8, 12] x10^{18} Pas Youngs mod [5, 10] GPa	MVO1 TRNT
VZ_{Max}	n	visco-elastic Maxwell depth-dependent	Expanding single ellipsoid with depth extension	Maxwell rheology: depth-dependent temperature, viscosity, elasticity see Fig. 13/14. E(z) reduced to 11 & 67% pressure/volume see Table 3	MVO1 TRNT
VZ_{SLS}	n	visco-elastic SLS depth-dependent	Expanding single ellipsoid with depth extension	SLS rheology: depth-dependent temperature, viscosity, elasticity see Fig. 13/14. E(z) reduced to 11 & 67% pressure/volume see Table 3	MVO1 TRNT

previous section as alternatives to continued magma influx, we return to volume-based sources, however employing now non-rotationally symmetries. We adopt the spherical source centred at 6 km depth and transform it into an expanding ellipsoid by varying the half axes and orientation systematically (Table 1) deriving at a geometry of semi-axes 1 km × 0.3 km × 1 km, volume 1.26 km^3, centred at 6 km b.s.l. and orientation of 263^0 (Model E_{1E}). This source model matches the observation of the distal GPS stations better than any rotationally symmetric source (Fig. 5, left). In order to include the data observed on the close GPS stations, a second, shallow deflating ellipsoidal source (Model E_{2E}) of semi-axes 500 m × 150 m × 150 m, volume 0.05 km^3, centred at sea level and an orientation of 293^0 (Fig. 5, right). The corresponding data misfits are 26.1 mm and 18.4 mm for models E_{1E} and E_{2E}, respectively. We refer to this set of volume sources as 'Initial Elastic Models' (see Table 1: E_{1E}, E_{2E}, and E_{1Ex}) and use them to explore in the following sections their compatibility with previous pauses and phases, their potential trade-off with depth, the impact of magma compressibility, and finally the potential impact of a visco-elastic crust in which these volume sources are embedded. All these strands of investigation focus on better quantifying the processes that cause the island – wide inflation of Montserrat or aim to find alternative explanations.

Assuming a homogeneous medium, Young's modulus of 10 GPa, and a Poisson's ratio of 0.25, a uniform inflation of 10 MPa per year for the deep source and deflation of 5 MPa per year for the shallow source is required to explain the surface deformation. Equivalent volume changes related to inflation and deflation are determined through eq. 1–5 in the next section and expressed as volume change rates by considering a time span of 10 years in Pause 5. Hence, 10 MPa/year and 5 MPa/year correspond to a uniform source volume change rate of 0.05 m^3/s and 0.003 m^3/s for the expanding deep source and contracting shallow source, respectively (Model E_{2E}).

4.4. Volume - pressure equivalence

Surface deformation due to a magmatic intrusion has been often modelled by a Mogi source (Mogi, 1958) where the intrusion is represented by a small, spherical cavity of radius a, embedded in an elastic half space at depth d. An isotropic stress is applied to the cavity wall which corresponds to the overpressure P exerted by the intrusion. The deformation at the stress-free surface is calculated in an iterative approach leading to a point source approximation ($a << d$) which is satisfied if $a < ½\ d$.

The corresponding volume change ΔV in the cavity can be approximated for a spherical geometry in an isotropically elastic half space by (McTigue, 1987)

$$\Delta V \approx \pi P a^3/\mu \tag{1}$$

with the shear modulus

$$\mu = \frac{E}{2(1+\nu)}, \tag{2}$$

Young's modulus E, and Poisson's ratio ν.

For a Poisson's ratio of $\nu = ¼$ this leads to a relative volume change

$$\frac{\Delta V}{V} = \frac{3}{4\mu} P \tag{3}$$

or

$$\frac{\Delta V}{V} = 1.875 \frac{P}{E} \tag{4}$$

For geometries used in our models (Models E_{1Ex}, Fig. 6) we have used an equivalent expression

$$\frac{\Delta V}{V} = k \frac{P}{E} \tag{5}$$

where k has been determined by numerical integration over the volumetric strain along the source geometry. For an ellipsoid $k = 3.5$, and for a depth-extended elliptical source geometry reaching a depth of 12 km and 14 km, $k = 4.8$ and $k = 5$, respectively. This allows us to convert pressure changes of different source geometries into equivalent volume changes of incompressible magma in a cavity embedded in an elastic half space as seen in the following section (Figs. 6 and 7).

4.5. Constraints on source volume and model trade-offs

Following the study by Christopher et al. (2015) that points to a larger magma reservoir under Montserrat, we have explored the parameter space by adding to our magmatic source at 6 km depth a deeper root (Model E_{2Ex}). We have increased the volume by extending it vertically through an insertion of additional volume below the upper

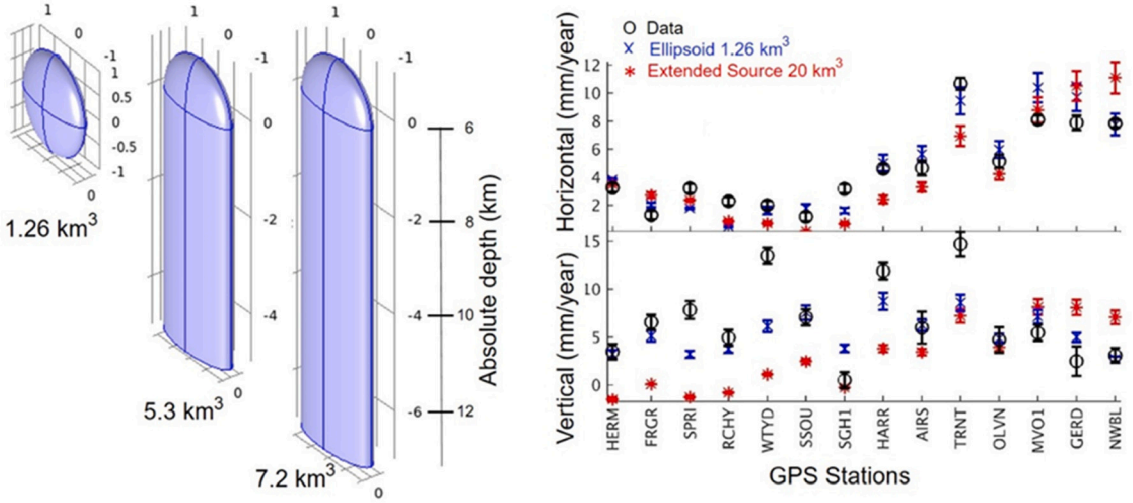

Fig. 6. Left, source geometry (E_{1Ex}): elliptical cross section 600 m × 2000 m; shown for depth range of vertically extended geometry by 5000 m and 7000 m, or total depth to 11,000 m and 13,000 m. Right: Impact of modelled vertically extended volume to the vertical and horizontal displacement of the Pause 5 data. The stations are listed in order of increasing horizontal distance from the volcano. Model results are illustrated for the initial ellipsoidal model with 10 MPa pressure and a source extended vertically up to 20 km^3 with a pressure of 3 MPa. The shallow deflating source remains the same for both models (Model E_{2Ex}). Using a large initial volume results in a large relative surface displacement at the more distal stations (MVO1, GERD, NWBL).

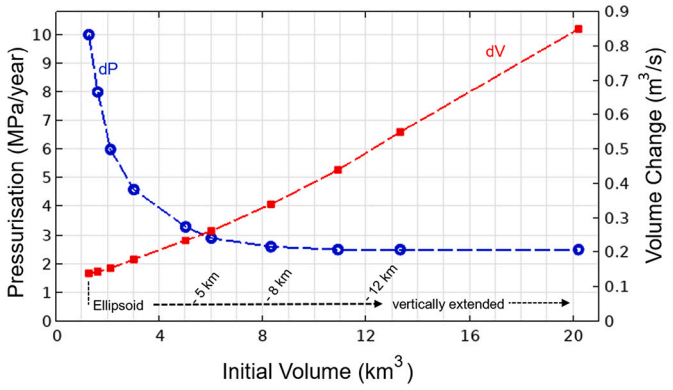

Fig. 7. Annual pressure increase (dP, blue) applied to the extended sources as shown in Fig. 6, and resulting volume change (dV, red) against initial volume. The pressure required to match the data converges to 2.5 MPa for sources extended to a volume in excess of 8 km^3. All data points (i.e. combinations of pressure increase and initial volume; blue dots) result in a similarly good data match. Increasing the initial volume beyond 8 km^3 yields a linear increase in volume change, while the equivalent annual pressure increase remains constant.

hemisphere of the elliptical source geometry, as depicted in Fig. 5. This maintains the shape of the top of the source controlling most of the closer surface deformation, but increases the depth to which the source can be pressurised, relevant for distal stations.

When extending the source vertically and reducing the pressure simultaneously we maintain an equally good match to the horizontal, distal GPS data, and an interesting pattern arises (Fig. 7): Once the source is extended vertically to a depth of 14 km and a total initial volume of about 8 km^3, the pressure increase required to match the Pause 5 data converges at about 2.5 MPa/year. This indicates a trade-off between source pressure and initial volume of a magma reservoir into which new magma could enter. The bigger this initial volume, the larger is the volume of magma influx, creating the same pressure increase and, consequently, the same deformation field. Hence, the estimate for a corresponding magma influx can vary from 0.14 m^3/s for an initial reservoir volume only 1.25 km^3 (ellipsoidal geometry in our initial model E_{1E}) to 0.85 m^3/s for a reservoir (E_{1Ex}) of about 20 km^3 (Fig. 7 – right hand axis). Assuming magma accumulation into a larger, initial reservoir as the only source process provides an upper bound of equivalent pressurisation of about 2.5 MPa/year. In general, this attempt to explore the depth – pressure trade-off also demonstrates why many other studies have used vertically extended ellipsoids in their models (Elsworth et al., 2014), and confirms the fact that geodetic data are not sensitive to vertical extensions of magma reservoirs.

4.6. Application to previous phases and pauses and impact of magma compressibility

Following Fig. 3, there is a remarkable similarity in displacement patterns between all the pauses and phases recorded at SHV. Using the initial model (E_{1E}) defined in 4.3, we go backwards in time and model the deflation during eruptive Phase 3, which can be matched by a depressurisation of about 40 MPa or a corresponding volume change of 17×10^6 m^3 at the deep source. The modelled volume changes for all phases and pauses until 2017 are summarised in Fig. 8, together with the estimated dense rock equivalent (DRE) volumes according to Wadge et al. (2014). Consequently, we can assume that the general source geometry must have remained stable through time with the GPS network measuring significant variations in magma volume or pressure. Note that there is a large discrepancy between modelled volume change at depth and estimated dense rock equivalent which can be accounted for by introducing a compressible magma at depth.

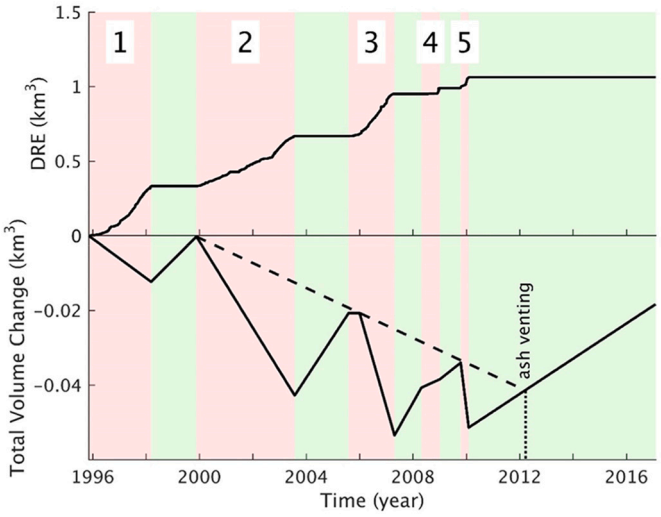

Fig. 8. Cumulative DRE volume erupted (adapted from Wadge et al., 2014) (top) and the change in total source volume through time relative to the start of the eruption (bottom). Total source volume change is based on the initial elliptical source volume (Model E_{1E}) of 1.26 km^3. The dashed line indicates the trend of eruption onsets for Phases 2, 3 and 5. The location of the March 2012 ash-venting event is indicated.

A negative or positive volume change within the source model corresponds directly to extruded or intruded incompressible magma from, or into a reservoir, respectively. However, due to its volatile content, magma is compressible which leads to discrepancies when comparing DRE of extruded material with pressure or volume changes at depth as indicated in Fig. 8. In order to reconcile this discrepancy between apparent volume change at depth derived from modelling the deformation field, and the erupted volume (DRE) during eruptive phases we have to consider the compressibility of magma at depth. The change in volume within the source region (V_M) can be linked to the estimated DRE volume (V_{DRE}) by applying conservation of mass (Segall, 2010)

$$\delta V_M = \delta V_{DRE} \left(\frac{\rho_{DRE}}{\rho_M}\right) \left(\frac{1}{1+\frac{\beta_M}{\beta_s}}\right), \tag{6}$$

where the DRE density (ρ_{DRE}) is 2600 kg/m^3 (Wadge et al., 2010), while β_s and β_M are the compressibility of source reservoir and magma, respectively (Table 2). The magma source density (ρ_M) has been calculated according to

$$\rho_M = \left[\frac{n}{\rho_g} + (1-n)\left(\frac{x}{\rho_c} + \frac{1-x}{\rho_m}\right)\right]^{-1} \tag{7}$$

(e.g. Huppert and Woods, 2002; Neuberg and O'Gorman, 2002). All variables have been defined in Table 2. Assuming water as the main volatile phase, we have used Henry's law of solubility to calculate the exsolved water content ($n = N - 4.11 \times 10^{-6}\sqrt{P}$), the gas density following the ideal gas law ($\rho_g = MP/RT$) with a total volatile content (N) of 4–6 wt% and crystal content (x) of 40% (Huppert and Woods, 2002). Edmonds et al. (2014) consider a larger total volatile content, however, with 6 wt% we take into account the effects of continued outgassing. The compressibility of the source magma (β_M) and magma reservoir (β_c) have been calculated as (e.g. Segall, 2010)

$$\beta_M = \frac{1}{\rho_M}\frac{\partial \rho_M}{\partial P} \text{ and } \beta_c = \frac{1}{V_M}\frac{\partial V_M}{\partial P} \tag{8}$$

respectively, and will be used in the following sections whenever magma at depth is being compared with DRE.

Table 2
Variables used in the compressibility calculations and deformation models.

Parameter	Description	
V_{Source}	Source Volume	m^3 (calculated)
V_{DRE}	Volume of erupted material (DRE)	m^3 (Wadge et al., 2010)
ρ_{DRE}	Density of erupted material (DRE)	2600 kg/m^3
ρ_M	Density of magma	kg/m^3 (calculated)
β_M	Compressibility of magma	Pa^{-1} (calculated)
E	Young's Modulus	1.3–12.2 GPa (Paulatto et al., 2019; reduced to 11% - 67%)
ν	Poisson Ratio	0.25
η	Viscosity	Pas (calculated)
β_s	Compressibility of source reservoir	Pa^{-1} (calculated) (Huppert and Woods, 2002)
β_r	Rock bulk modulus	$E/3(1- 2\nu)$
n	Exsolved gas content	wt% (calculated)
N	Total gas content	4–8 wt%
ρ_g	Gas density	kg/m^3 (calculated)
ρ_c	Crystal density	2600 kg/m^3
ρ_m	Melt density	2300 kg/m^3
x	Crystal content	40%
M	Molecular mass of water	0.01801528 kg/mol
P	Pressure	Pa (calculated)
R	Universal Gas content	8.314 J/mol K
T	Temperature	300–1350 K
dT/dz	Thermal Gradient	0.03–0.1 K/m
A	Dorn Parameter	5×10^9–10^{10} Pas
H	Activation Energy	1.06×10^5 - 2.17×10^5 J/mol

4.7. Summary of elastic models

Fig. 5 depicts a reasonable match between data and our models E_{1E} and E_{2E} based on a homogeneous, elastic crust below the Montserrat topography. Maintaining the shallow ellipsoidal source (E_{2E}) is needed to force the horizontal displacement of the three close stations to point inwards. The vertical displacements are less well fitted when we use vertically extended sources as those can result in a trade-off between horizontal and vertical displacement. A classic example is the displacement field of a dyke that results in a negative vertical displacement above the dyke which increases with the amount of dyke opening while a positive horizontal displacement prevails in the far field. Dieterich and Decker (1975) have demonstrated that, in order to constrain the source geometry perfectly, both horizontal and vertical components are needed, however this is not the aim of this study. By introducing more model parameters, either by refining the geometry or by introducing a two- or even three-dimensional elastic model the data fit could be further improved. This has been achieved by several previous studies which were all based on an elastic response to magma influx or drainage (e.g. Elsworth et al., 2008; Hautmann et al., 2010; Foroozan et al., 2011). Our attempt to explore the depth – pressure trade-off in Section 4.5 demonstrates why many other studies have used prolate spheroids in their models. A comprehensive summary of previous model attempts, with their different settings and parameters, advantages and shortcomings has been presented in Elsworth et al. (2014). In contrast, we set out to compare different *conceptual* and *contrasting* models that explain the ongoing inflation of Montserrat and the eruption potential in the near future, rather than adding another purely elastic model to the collection. First, we considered and then excluded dykes and faults as a tectonic component of deformation. Second, we introduced geometries with non-rotational symmetry, and finally, we move in the following to visco-elastic models (Models V_H, VZ) and focus on the distal stations only. We drop the shallow elliptical source in our considerations as it only affects the closer stations (see Fig. 5), the deformation data of which might be masked by loading effects (Odbert et al., 2015) rather than revealing deep source processes we are interested in. We use in the following the depth-extended ellipsoidal geometry (same as Model E_{1Ex} and depicted in Fig. 6) with an initial volume of about 8 km^3.

5. A visco-elastic model for the Montserrat eruption

In the previous sections we ruled out tectonic sources and dykes as sole deformation sources and established a source geometry which, applied to volume or pressure changes can explain the deformation data on Montserrat throughout the course of the eruption. The choice of an elliptical geometry in contrast to an isotropic, rotational symmetry or a more realistic, detailed crustal model is not vital compared to the fundamental question whether the volcanic system of Soufrière Hills volcano is further pressurising by continued magma influx or other pressurising mechanisms, or volcanic activity is finally declining, even at depth. So far, the deformation pattern has been interpreted as a magma drainage and extrusion for phases, and renewed magma influx or pressurisation for pauses; in the following we test a hypothesis to re-interpret the inflation pattern during pauses in a fundamentally different way.

5.1. Petrological indications for the end of a magma intrusion

The recent study by McGee et al. (2019) has provided a strong suggestion that the magma intrusion below SHV might have ended sometime in 2004 (from Phase 3 onwards), based on a comparison of mafic enclaves and andesitic host rock over the entire period between 1995 and 2010. They used the short-lived isotopes ^{210}Pb and ^{226}Ra in the Uranium series decay chain as an indicator for volatile transfer and loss in both the enclaves and the host andesite to reveal significant changes over time. While erupted andesite has been almost entirely in equilibrium or has shown deficits of ^{210}Pb indicating continuous volatile loss before and throughout the eruption, most of the mafic enclaves have shown an excess of ^{210}Pb, interpreted as volatile enrichment that has lasted over a decade. The highest $^{210}Pb/^{226}Ra$ ratios have been determined from enclaves in Phase 2, decreasing continuously afterwards. This pattern has been explained by a cutting off fresh gas influx in the deeper mafic system from Phase 3 onwards. The ^{210}Pb excess can be modelled by one single, extended intrusion of basaltic magma at depth (carrying fresh gas), probably intruded in 1992 coinciding with the occurrence of deep seismicity. Hence, the intrusion might have ended with Phase 2, when the gas influx decreased preventing further build-up of ^{210}Pb.

5.2. Generalised Maxwell rheology

Visco-elastic models have been employed by several studies (e.g. Del Negro et al., 2009; Gottsmann and Odbert, 2014; Hickey et al., 2016), and a comprehensive overview on rheological models can be found in Head et al. (2019). Based on the petrological considerations in the previous section we have contemplated an alternative explanation for the inflating deformation patterns during pauses as the ongoing response of a viscous crust to an initial intrusion from 1992 through 2003, excluding any additional magma influx afterwards. We use the 'saw-tooth' deformation pattern in the iconic MVO overview plot depicted in Fig. 2 and refer to the behaviour of the distal stations (MVO1 and NWBL) as they are most strongly indicative for the processes of the deeper magmatic system. Striking features that have guided our modelling attempts are the slightly declining steepness of inflation during pauses while the deflation phases show a steepening trend. Furthermore, we have recognised an almost perfect linear behaviour in both phases and pauses that suggests a visco-elastic behaviour represented by a Maxwell rheology illustrated in Fig. 9.

A Maxwell rheology is characterised by a viscous- and an elastic element in series where ε_e and ε_v are the elastic and viscous strain responses, respectively, at $t > t_o$ to a step-like pressure pulse ΔP at time $t = t_o$. The total strain response is given by adding these components

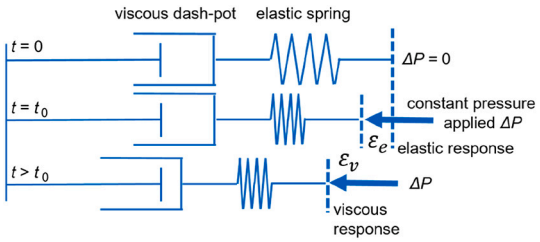

Fig. 9. Three stages of visco-elastic response using Maxwell rheology; system in equilibrium at $t = 0$, pressure step ΔP at time t_0, long-term response for $t > t_0$.

$$\varepsilon_{\text{total}} = \varepsilon_{\text{e}} + \varepsilon_{\text{v}}, \tag{9}$$

or in terms of pressure.

$$\varepsilon_{\text{total}}(t) = \frac{\Delta P}{E} + \frac{\Delta P}{\eta}\, t \tag{10}$$

where E is Young's modulus and η the viscosity. Depending on the dimension, direction and the medium considered E can be replaced by rigidity (shear modulus) or incompressibility (bulk modulus), and accordingly, η can be either shear or bulk viscosity. Eq. 10 implies an immediate, time-independent elastic response, and a viscous response that is linear in time and continuous as long as the pressure ΔP is applied. In our case the elastic parameter is the shear modulus μ and η the shear viscosity.

The Generalised Maxwell model comprises several Maxwell branches and in addition a parallel, purely elastic branch where the elasticity value is partitioned between all branches. In its simplest form the generalised model consists of only one Maxwell- and one elastic branch and is referred to as Standard Linear Solid (SLS) where elasticity is partitioned as μ_1 and μ_2 (Fig. 10). This results in strain patterns that react

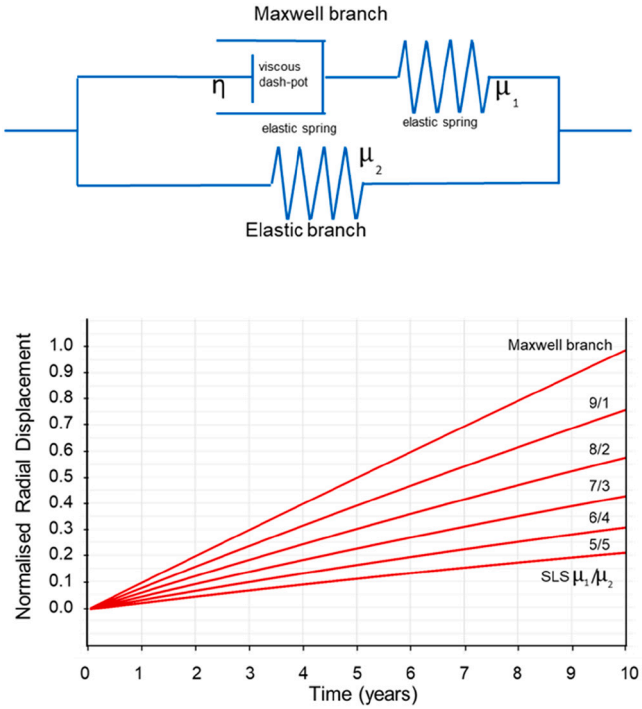

Fig. 10. Comparison between Maxwell rheology and SLS with varying elasticity partitioning μ_1 and μ_2. While the pure Maxwell branch has a linear time dependence here depicted for 10 years (see Eq. 10), the SLS reduces the amplitude and shows a curved trajectory due to the retardation time τ and parameters within (see Eq. 11 and 12). This example is based on Young's modulus E = 10 GPa, pressure step dP = 20 MPa, and viscosity $\eta = 10^{19}$ Pas.

to pressure changes with a delayed response, the characteristic timeτ, which is dependent on the choice of viscosity and elasticity partitioning. Hence, the linear time-dependent response of the Maxwell rheology is replaced by.

$$\varepsilon_{\text{total}}(t) = \frac{\Delta P}{\mu_2}\left(1 - \frac{\mu_1}{\mu_1 + \mu_2}\, e^{-\frac{t}{\tau}}\right) \tag{11}$$

with the characteristic (retardation) time.

$$\tau = \eta \frac{\mu_1 + \mu_2}{\mu_1\, \mu_2}. \tag{12}$$

While the partitioning of the elastic modulus between the two branches offers an additional degree of freedom to fit observational data, the two elasticity values lose their original physical meaning. Lin (2020) describes this split of elasticity into two branches by an additional parameter $g = \mu_1/(\mu_1 + \mu_2)$, that varies between 0 and 1, governing the ratio of viscous fluids to solids in a visco-elastic solid, e.g. partial melt to solid rock. As a consequence, the choice of μ_1 and μ_2 might be depth/temperature-dependent but is often kept constant as $\mu_1 = \mu_2 = 0.5\,\mu$ (e.g. Del Negro et al., 2009; Head et al., 2019).

Fig. 10 shows the impact of the choice of μ_1 and μ_2 in comparison with the Maxwell rheology; progressive partitioning between μ_1 and μ_2 results in reduced amplitudes of deformation, for high viscosities the SLS converges to a purely elastic system. A higher pressure is necessary in an SLS (compared to a Maxwell rheology) to explain the same deformation. Hence, Maxwell- and a purely elastic model are endmembers bracketing the range of pressures to explain the amplitude of a deformation pattern. By considering these endmembers in realistic visco-elastic parameter distributions we have attempted to gain insight into upper and lower bounds of magma influx or pressurisation.

Given the intriguingly linear behaviour and the abrupt changes between pauses and phases in the deformation pattern, we start to explore the parameter space with a pure Maxwell rheology (Fig. 9) in a simplified model with homogeneous viscosity η and Young's modulus E, describing the visco-elastic crust surrounding the magma (Model V_h). In this case the linear behaviour during pauses is only dependent on shear viscosity and the residual reservoir pressure once magma extrusion has stopped while phases are also governed by shear modulus and the decreasing pressure caused by volume loss during the phases. The model setup comprises the vertically extended ellipsoid of Fig. 6 (same as Model E_{1Ex}) embedded in a homogeneous half space. Following this approach we have derived a set of homogeneous models that equally match the deformation pattern (see Fig. 11) using viscosities in the range of $\eta = [1.8 \times 10^{18}, 1.2 \times 10^{19}]$ Pas and a Young's modulus ranging $E =$ [5,10] GPa.

According to Eq. 10, the linear trend we have seen in Pause 5 which we have attempted to interpret as a visco-elastic response to an initial magma intrusion rather than as a continued, buoyant magma influx, is only dependent on constant pressure and the viscosity, which in turn is controlled by the crustal temperature distribution. To keep the residual pressure constant during a pause we have assumed the modelled magma intrusion to be connected to a larger, deeper reservoir such that the small volume change due to inflation can be compensated by mass transfer from the reservoir. Magma compressibility plays an additional role in pressure recovery and inflation as discussed by Segall (2016).

In the following we explore the wide range of depth-dependent temperature and resulting viscosities and their influence on the deformation models.

5.3. Temperature and viscosity dependence

The exact temperature distribution on Montserrat is controlled by several factors such as hydrothermal activity and the accurate location and history of the magma intrusion, which is subject to large uncertainties. These large uncertainties are also reflected in the literature:

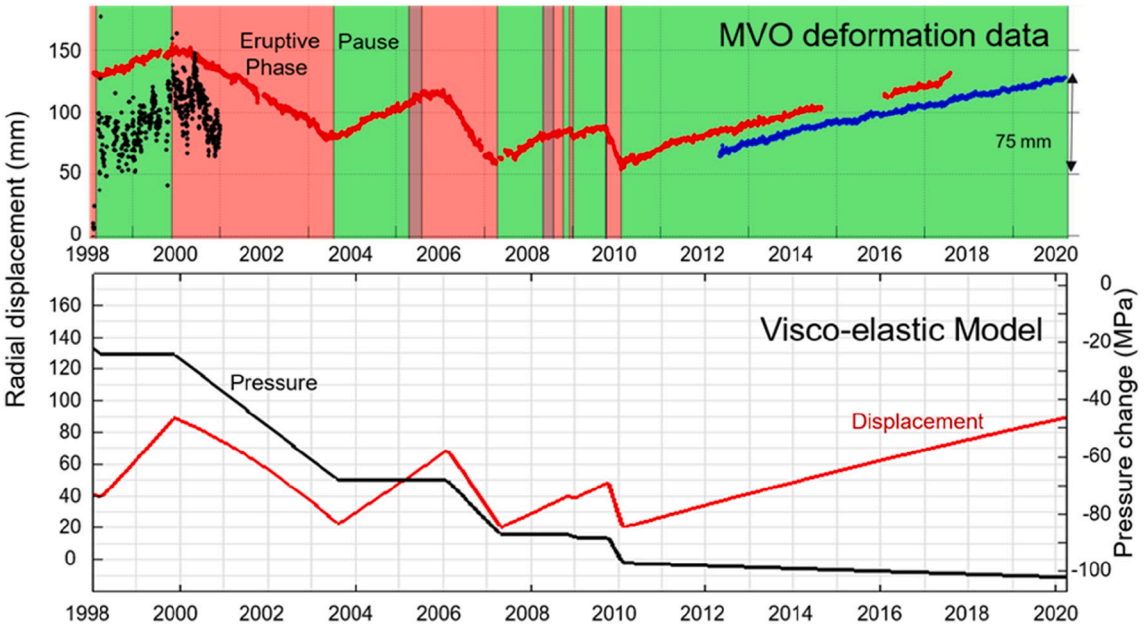

Fig. 11. Comparison of the radial deformation at station MVO1 (upper panel, from Fig. 2) with the modelling results (lower panel) for the same station as a visco-elastic response using a Maxwell rheology (Model V_H). Results are shown for a constant Young's modulus of 10 GPa, a constant viscosity of 3.3×10^{18} Pas, and a depressurisation and reservoir volume change equivalent to 100 MPa. Note that in this model a slight change in the deformation gradient in Pause 5 is achieved by a small pressure decrease during the pause.

Manga et al. (2012) measured temperature gradients near the seafloor in the Lesser Antilles and found values between 0.06 K/m, and up to 0.1 K/m in a borehole at the arc crest between Montserrat and Guadeloupe at a water depth of 1200 m and borehole depth of 280 m. Geothermal investigations on Montserrat found temperatures of 200° C (473 K) at 2000 m depth over a wide area surrounding the volcanic centre (Ryan and Shalev, 2014) leading to a shallow temperature gradient of 0.1 K/m. Gottsmann and Odbert (2014) implemented in their models an island-wide crustal hot zone of 1373 K between 31 km and 27 km depth superimposed to an elevated crustal heat flow modelled by one or two crustal magma reservoirs. Similar to Gottsmann and Odbert (2014), we have implemented a thermal model, based on the source geometry we found in Section 4 for the intrusion, which is underpinned by a deeper magma reservoir between 14 and 20 km depth (e.g. Zellmer et al., 2003). This deeper reservoir does not have any impact on the surface deformation which is controlled by the deep-rooted intrusion modelled by the extended ellipsoid above. We use a temperature of 900 K at 20 km depth, and 1350 K in the deep reservoir and intrusion. This corresponds to thermal gradients of 0.075 K/m above the deep reservoir and 0.03 K/m further away from reservoir and intrusion.

The Arrhenius approximation has been widely used to estimate shear viscosity $\eta(T)$ distributions from depth-dependent temperature models (e.g., from basaltic magmas, Del Negro et al., 2009; to silicic compositions, Le Mével et al., 2016).

$$\eta = A\, e^{\left(\frac{H}{RT}\right)} \tag{13}$$

where A is the Dorn parameter, H is the activation energy, R is the ideal gas constant, and T is temperature in degrees K. Recent visco-elastic studies have employed commonly used values for A and H that are potentially representative of the geochemical composition and subsurface temperature. In contrast, Morales Rivera et al. (2019) have explored the full range of these parameters by applying thermo-mechanical models to the 2010–2011 unrest of Taal volcano, Philippines, investigating how host rocks with distinct viscosity endmembers in the Arrhenius formulation affect the response of the Earth's surface due to magma reservoir pressurisation. In their study they used a range of activation energies H between 106 kJ/mol to 217 kJ/mol, respectively, equivalent to a silicic and intermediate crust. Using Eq. 13 leads to a range of viscosities spanning several orders of magnitude for the same crustal temperature of 600 K. In the same study the Dorn parameter A is varied between 5×10^9 and 2×10^{13} Pas, again for a silicic and intermediate crust, adding another 4 orders of magnitude difference for the same temperature. These examples demonstrate how large the uncertainties in both temperature, and consequently in viscosity are.

For the next modelling step we have chosen values for the Dorn parameter $A = 10$ GPas, and the activation energy $H = 120$ kJ/mol previously used for Montserrat (e.g. Odbert et al., 2015) and derive the viscosity distribution depicted in Fig. 12A. We have estimated a range of potential temperature and corresponding viscosity values by profiling the area that contributes most to the deformation field below the station MVO1. These profiles and the resulting average viscosity values are depicted in Fig. 12B for the distal station MVO1. All profiles converge towards the surface to viscosity values far above the range we employed in our simplified homogeneous model. Therefore, we have tested the endmember models by Morales Rivera et al. (2019) in the Arrhenius formulation Eq. 13 to find the lowest value possible for a corresponding endmember in viscosity. This viscosity distribution (Fig. 12D) is then used to compute the deformation pattern as a response to an initial intrusion without any further pressurisation or magma influx. We refer to this viscosity distribution and Young's modulus profile derived from Paulatto et al. (2019) and reduced to 67% and 11% (Gudmundsson, 1990) as explained in Section 3, as the 'depth-dependent model', VZ_{Max} and VZ_{SLS}, hereafter.

5.4. Visco-elastic response to magma intrusion

Using the Maxwell rheology introduced in Section 5.2 and the viscosity distribution derived in Section 5.3 we can now model the visco-elastic response to an initial intrusion that is followed by a stepwise depressurisation of a magma reservoir due to extrusion of magma during Phase 2 through Phase 5, using the same pressure steps as employed in the homogeneous model V_H (Fig. 11). We present in Fig. 13 the corresponding radial deformation for GPS station MVO1 for a pure Maxwell

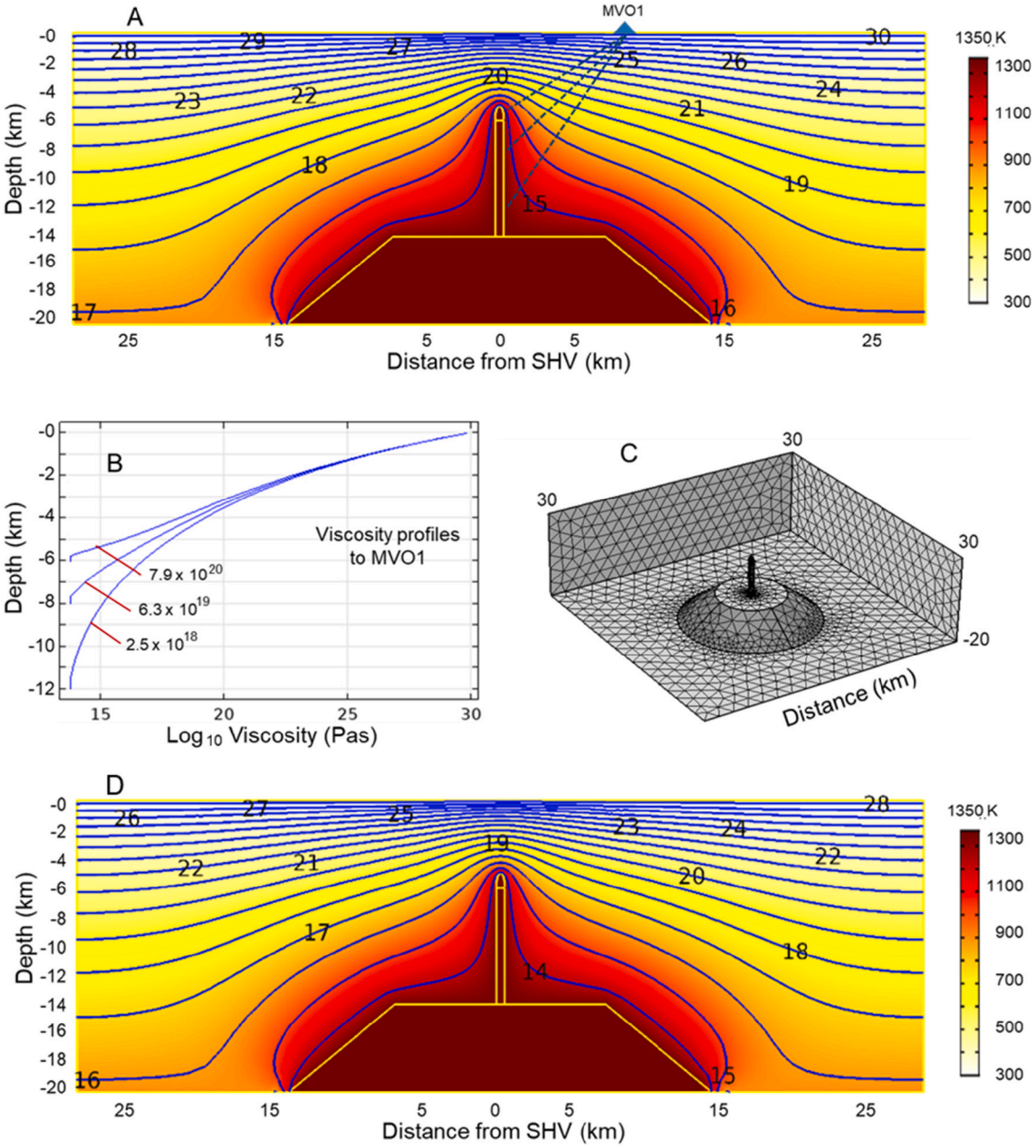

Fig. 12. Temperature – viscosity model VZ_{Max}. A: temperature distribution and contoured viscosity values (Log_{10}). Dashed lines indicate where viscosity profiles have been calculated between the magmatic source at different depths and distal GPS station MVO1. B: Viscosity profiles between MVO1 and magmatic source at 12, 8 and 6 km depth. Viscosity averages over the profiles are indicated. C: Meshed temperature model comprising cone shaped deep reservoir (30 km wide and 6 km high) and superimposed magma intrusion as depicted in Fig. 6 left. D: endmember model for lowest possible viscosities which differ from (A) by one to two orders of magnitude.

rheology (VZ_{Max}), several SLS rheologies (VZ_{SLS}) and a purely elastic model for reference (E_{1Ex}). In contrast to the homogeneous model V_H in Fig. 11 the deformation during the pauses when the pressure stays constant does show a small inflationary trend for the Maxwell rheology (Fig. 13A) which is in the same order of magnitude as the observation. However, this inflationary trend is much smaller than the deflation during magma extrusion resulting in an overall deflation which follows the pressure profile over time, unlike the observed saw-tooth pattern in Figs. 2 and 11. In fact, the small inflationary trend is well explained by the dissipation of crustal stress exerted by the initial intrusion. The more realistic depth-dependent model reveals the interaction between regions of different properties. Here elastic energy is stored in layers with high viscosity after the initial pressurisation and then dissipated due to the viscous behaviour of regions with lower viscosity. This behaviour has been previously noted and modelled by other studies (e.g. Yamasaki et al., 2017) and is demonstrated in Fig. 13C depicting the crustal response to a positive pressure step of 20 MPa for Maxwell and SLS rheology over 10 years. Here the homogeneous visco-elastic model V_H (Fig. 11) is replaced by the same depth-dependent, visco-elastic model used VZ_{Max} for Fig. 13A. Unsurprisingly, the SLS rheology (VZ_{SLS}) follows closely the pressure profile and the purely elastic behaviour without any inflation trend during pauses (Fig. 13B).

We started from a simplified homogeneous model V_H (Fig. 11) where we determined a viscosity-elasticity combination that could explain the 'saw-tooth' pattern observed in Fig. 2. Despite using endmember viscosity profiles as close as possible to the low viscosities of the homogeneous model, the 'saw-tooth' pattern cannot be reproduced by pauses during which the pressure remains constant. Hence, we have to reject

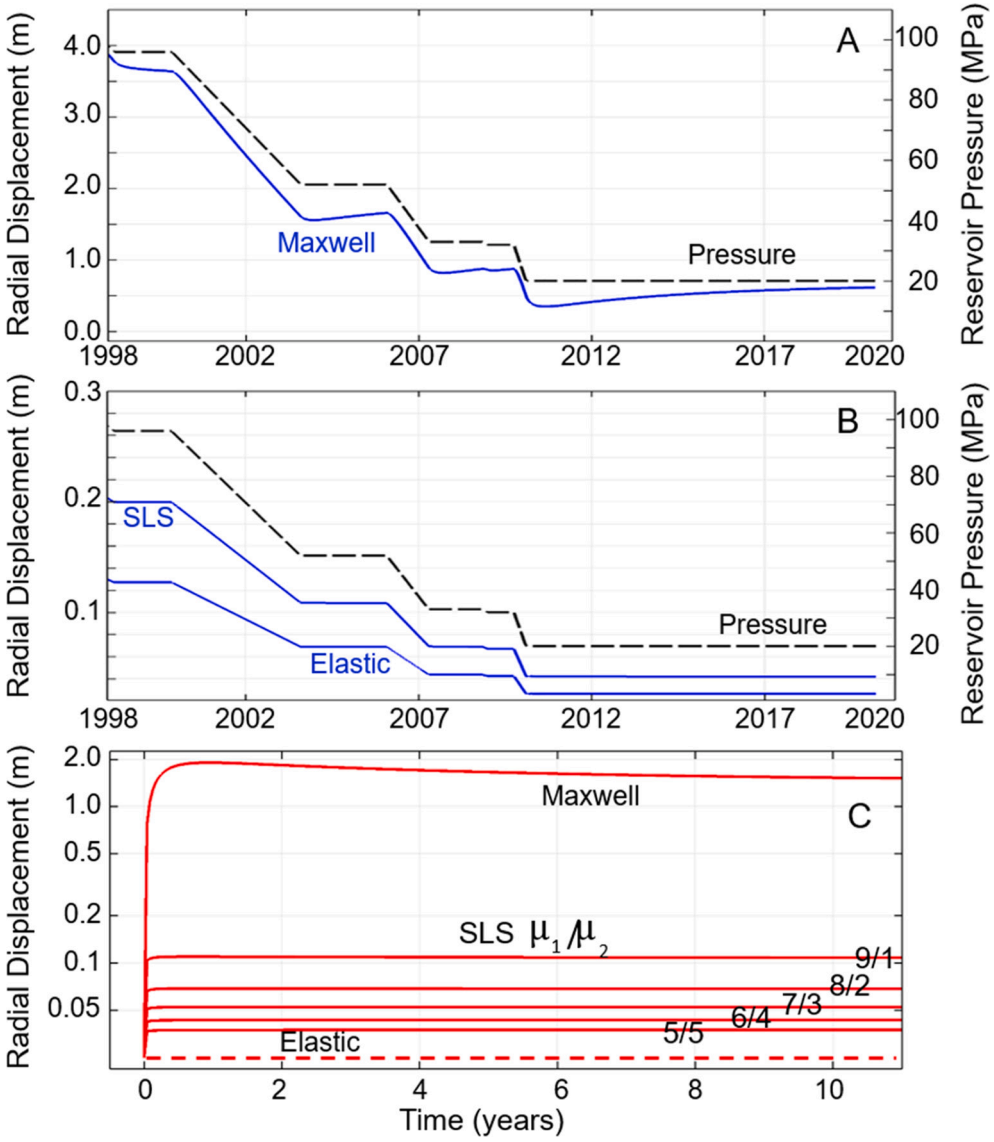

Fig. 13. A: Pattern of radial deformation at MVO1 for depth-dependent visco-elastic model derived in Section 5.3 and Maxwell rheology (VZ_{Max}) using the same depressurisation steps as in the homogeneous model (V_H) in 5.2. B: same for SLS rheology. C: Response of depth-dependent model used in A to a positive pressure step of 20 MPa for different rheology models. Note the logarithmic amplitude scale.

the hypothesis that the inflations during pauses, particularly the ongoing inflation that has continued for more than 10 years, can be explained by a delayed crustal response to an initial intrusion without any further magma influx or pressurisation.

6. Discussion

Based on the elastic models of Section 4 we have re-introduced pressurisation during pauses in the following set of numerical models, and have estimated to what extent such pressurisation can be reduced by visco-elastic rheologies developed in the previous section. Using purely elastic behaviour, SLS and the Maxwell rheology we have attempted to find endmembers of pressurisation values, for which we discuss potential physical processes that explain the observations in Pause 5.

6.1. Final numerical deformation models

The modelling results displayed in Fig. 14 have been obtained by applying the same pressure values and history as depicted in panel A, hence, resulting in different radial displacements according to the choice of rheological model. By scaling these radial displacements to the observations throughout the eruptive history we have determined the time line and values for pressurisation and depressurisation that correspond to the observations. We drop the extreme case in panel C (Fig. 14) for a Maxwell rheology combined with an elasticity value reduced to 11% as the overall temporal pattern does not fit the observations. All pressure differences throughout the eruption are listed in Table 3. Focussing on Pause 5 we obtain pressurisations dP/dt ranging from 0.1 MPa/year to 6 MPa/year for Maxwell (VZ_{Max}) and purely elastic case (E_{1Ex}), respectively.

The corresponding volume changes are determined by the volumetric strain integral over the intrusion (geometry Fig. 7) during inflation and result in 0.11 m^3/s to 0.57 m^3/s or 3.5×10^6 m^3/year to 18×10^6 m^3/year for the elastic and Maxwell case, respectively. As expected, the corresponding values for the SLS rheology are closer to the elastic case (Table 3).

6.2. Mass balance for compressible magmas

According to Wadge et al. (2014), Phase 3 involved the extrusion of

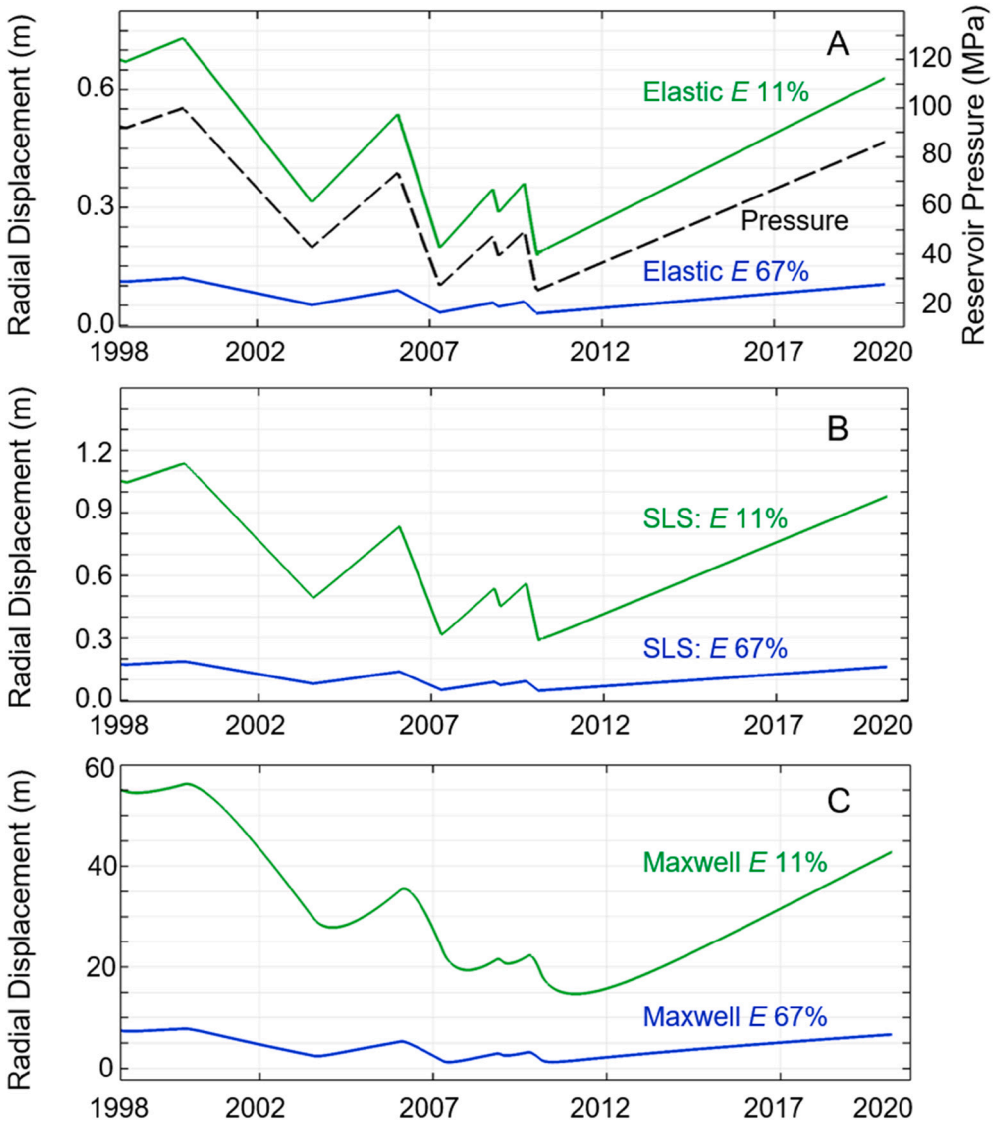

Fig. 14. Radial displacement at station MVO1 for indicated rheology and Young's modulus. E 11% and E 67% refer to the revised seismic velocity depth profile of Paulatto et al. (2019) reduced to 11% and 67%, respectively, as explained in Section 3. In all cases the same pressure history has been applied. A: purely elastic cases, B: SLS with equally shared shear modulus $\mu_1 = \mu_2$, C: Maxell rheology. Note the different scales in A, B and C.

282×10^6 m^3 DRE (Table 3). This is a factor of about 10 times larger than the volume change derived for an elastic model E_{1Ex} and twice the volume for a visco-elastic Maxwell model VZ_{Max}. However, this can be accounted for by the effect of magma compressibility at reservoir pressures (see Table 4). Using Eqs. (6) through (8) in Section 4.6 we estimate the equivalent, depth dependent volume changes for compressible magma with a 40% crystallinity and volatile content of 4–6 wt%; in Fig. 15 results for Phase 3 and Phase 5 are compared.

The modelled volumes for Maxwell and the elastic case are the output of the volumetric strain integral over the entire depth range displayed as horizontal lines while the DRE equivalent volumes corrected for compressibility due to 4–6 wt% H_2O content are given as depth-dependent. This shows that four times more material was erupted during Phase 3 compared to Phase 5. The elastic model underestimates the volume change at reservoir level for Phase 3 while the visco-elastic model appears to slightly overestimate the volume change at reservoir level for Phase 5. This could point to a decrease of volatile content in the remaining magma during the years between 2006 (Phase 3) and 2010 (Phase 5) causing a decrease in compressibility. Alternatively, this could also be interpreted as a continued influx of magma during extrusion for Phase 5. However, both elastic and visco-elastic models match in general the estimated DRE volumes once compressibility is taken into account and suggest that the models brace the realistic set of parameters that explain the deformation pattern throughout the eruption.

The apparent volume changes obtained through our numerical models need to be translated into DRE volumes according to eq. 6 in section 4.6 to reflect the actual mass of magma intruded into the reservoir. The factors ρ_{DRE}/ρ_m and $(1+\beta_m/\beta_c)^{-1}$ in Eq. 6 represent the effects of compressibility of magma and reservoir, respectively. Hence, using the volumes for Phase 5 in Table 3 and the apparent volume change rates in Table 2, we obtain correction factors of 5.7 and 2.6 for the elastic and Maxwell case, respectively. Applying those to the apparent volume change rates we finally obtain 0.62 m^3/s to 1.48 m^3/s or 19×10^6 m^3/year to 47×10^6 m^3/year for the elastic and Maxwell cases, respectively.

6.3. Link to SO_2 outgassing

Focussing on Pause 5 and the ongoing inflation of the island of Montserrat, another way to constrain the assumption of continuing magma influx as an explanation is a comparison with the outgassing of SO_2. Both traverse-based and network data acquisition place the amount

Table 3
Pressure changes for different models that explain the deformation patterns at MVO1 for all phases and pauses. The last three rows show the corresponding pressurisation rates and volumetric strain changes during Pause 5.

Phase/Pause	Estimated DRE (10^6 m^3) (Wadge et al., 2014)	Pressure change (MPa) Elastic models *E* reduced to		Pressure change (MPa) SLS models *E* reduced to		Pressure change (MPa) Maxwell model *E* reduced to 67%
		11%	67%	11%	67%	
1	331	−1	−8	−1	−5	−0.1
1		1	8	1	5	0.1
2	336	−9	−57	−7	−37	−0.7
2		5	30	4	20	0.3
3	282	−8	−46	−5	−30	−0.6
3		4	20	2	13	0.3
4	39	−2	−8	−1	−5	−0.1
4		2	10	1	7	0.1
5	74	−4	−24	−2	−16	−0.3
5		10	61	6	−39	0.8
d*P*/d*t* [MPa/year]		1	6	1	4	0.1
d*V*/d*t* [m^3/year]		3.5×10^6		4.2×10^6		18×10^6
d*V*/d*t* [m^3/s]		0.11		0.13		0.57

Table 4
Deep source volume change from our elastic (E_{1Ex}) and visco-elastic models (VZ_{Max} and VZ_{SLS}) compared to estimated DRE volumes (± 50%) from Wadge et al. (2014). Model parameters correspond to those used in Fig. 14.

Phase/Pause	Estimated DRE (10^6 m^3)	Volume change (10^6 m^3) Elastic model	Volume change (10^6 m^3) SLS/Maxwell
1	331	-5	-5/-13
1		5	5/22
2	336	-33	-39/-190
2		18	20/69
3	282	-27	-31/-122
3		12	13/25
4	39	-5	-5/-8
4		6	7/15
5	74	-13	-15/-29
(10 years) 5		35	42/180

of outgassed SO_2 in the range of 300 ± 130 t/day (Stinton et al., 2020).

Crystallisation during cooling (second boiling) reduces the volume of melt and, therefore, increases the vapour pressure forcing volatiles to exsolve and form bubbles. Even a partial confinement of these exsolved volatiles results in pressurisation of the magma reservoir, and hence, will contribute to the deformation field. If we assumed crystallisation as the sole mechanism to explain the deformation data and made the rather extreme assumption of a closed system where no exsolved gas can escape, a source volume of 40 km^3 would be required (Caricchi and Simpson, 2015) to generate the amount of gas needed matching a pressurisation of 1–6 MPa/year. While this volume is in agreement with the magma volume suggested by Christopher et al. (2015), it is significantly larger than our modelled sources ranging from 1.26 km^3 to 8 km^3, and the amount of volume generated by a uniformly degassing magma body of 40 km^3 would have to be concentrated in the upper part of our modelled intrusion in order to match the observed deformation data. Furthermore, the assumption of a sealed system seems unrealistic given the constant outgassing of SO_2 at 300 t/day during Pause 5, and we conclude that crystallisation induced degassing can only account for a very small fraction of the observed deformation data.

If we assume an open system and hypothesise that the entire amount of sulphur originates from a continuous influx of more mafic magma into a shallow intrusion we can obtain an upper bound of magma influx that is constrained by the long-term average of SO_2 output. Edmonds et al. (2014) estimated the amount of sulphur gases emitted continuously between July 1995 and July 2011 at $4.0 \pm 0.6 \times 10^9$ kg while the total amount of magma erupted in 5 phases during this time amounted to 1.1 km^3 (Wadge et al., 2010). Having found very little sulphur (<100 ppm) in melt inclusions, Edmonds et al. (2014) assumed that all of the sulphur emitted continuously over these years had resided as a volatile phase in the andesitic magma reservoir prior to the onset of eruption. Adopting the numbers by Edmonds et al. (2014) above, and assuming a magma density of 2600 kg/m^3, we estimate the sulphur content at about 0.14 wt %. Using the postulated volume influx in the range $dV/dt = [0.62, 1.48]$ m^3/s, this results in a magma mass influx of $dM/dt = [139, 332]$ x 10^6 kg/day, of which sulphur contributes 0.14 wt%. Hence we derive [195, 465] x 10^3 kg/day of sulphur or about [390, 930] t/day of emitted SO_2 based on our purely elastic model or the visco-elastic Maxwell model, respectively. These results are higher but overlap with the uncertainties of the measured outgassing of 300 ± 130 t/day and indicate that values of 1.48 m^3/s or 47 × 10^6 m^3/year form indeed an upper bound of magma influx into the deep reservoir.

7. Summary and conclusions

We embarked on an attempt to explain the current deformation pattern on Montserrat showing since 2010 a continuous expansion of the entire island, which has important implications in terms of understanding the future eruption potential of the volcano. We made use of the remarkable similarity of deformation patterns that can be applied to both inflation and deflation, hence one source geometry can be used for the entire eruptive history. Through numerical modelling we have matched GPS data sets to a deep source embedded in an elastic half space. Unlike other studies it has not been our intention to match all details of the deformation data which can be achieved by varying parameters like viscosity, elasticity, temperature in three dimensions. In contrast, we have explored alternative models as proof of concept. Prompted by the petrology study of McGee et al. (2019) that suggested the end of an initial magma intrusion by 2003, we have explored a set of visco-elastic models, testing whether the entire deformation pattern throughout the eruptive history can be explained by a visco-elastic response of the volcanic system to an initial intrusion without any further pressurisation during eruptive pauses. Rather than searching for one possible explanation, we attempted throughout this study to capture the widest possible range of modelling parameters in order to assess the range of possible solutions that could explain the deformation pattern on Montserrat.

- In our initial modelling attempts (Model I_S, I_D and I_F) we ruled out a dyke or fault to explain the deformation on Montserrat. Given the fact that there is little evidence for significant recent activity on the local faults as discussed in Section 4.2, we adopt a more realistic tectonic contribution of max. 3 mm/year in each direction (Wadge et al., 2014) which would correspond to a pressure reduction by only 1 MPa at the deep source geometry. Hence, we conclude that any tectonic contribution to the current deformation field has by comparison a very small impact.
- We conclude that the ongoing deformation pattern (Pause 5) is best explained using a dual-source model (Model E_{2E}/E_{2Ex}) with a shallow deflating source and a deeper inflating source. In terms of understanding the future eruption potential of the volcano, continuous magma accumulation is the main consideration, therefore, it is the deeper, inflating source which is more important. However, the deflating source suggests a depressurisation at shallow depths. The observation that the shallow source is not evident in the GPS data for any other phase or pause, other than Pause 5, implies it represents either a change in source process, or an ongoing process, the effects of which were previously masked by the deeper source. Potential

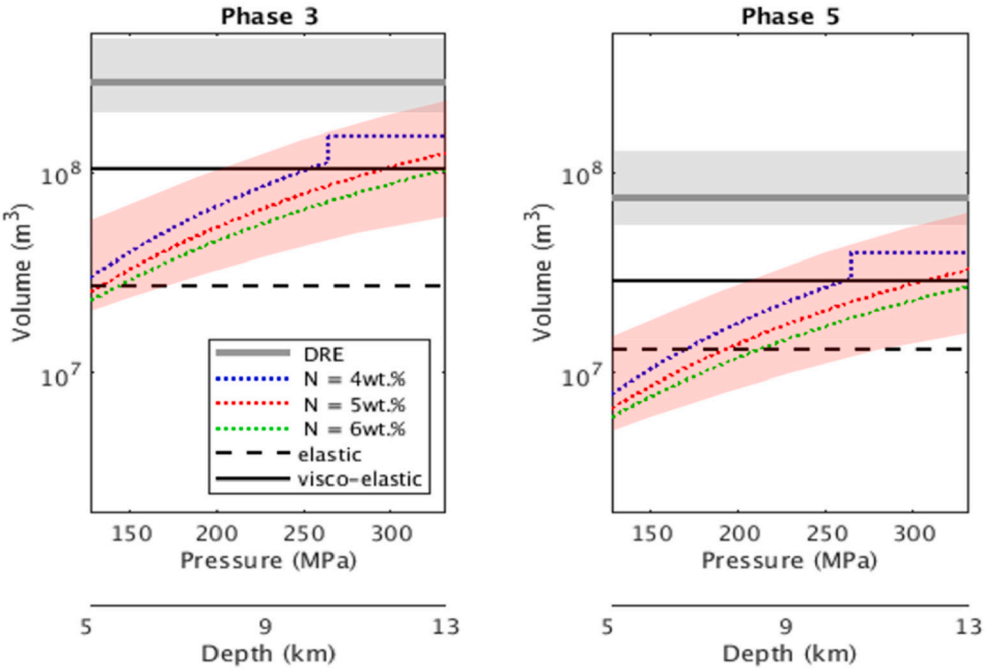

Fig. 15. Comparison between the estimated DRE volume and the modelled source volume change during Phases 3 and 5 for an elastic model (dashed black line) and a visco-elastic Maxwell model (solid black line). These volume changes are based on the modelled GPS data listed in Table 2 integrated over the depth range between 5 and 13 km. Dotted lines are corresponding, depth-dependent volumes corrected for magma compressibility for different initial gas contents (4–6 wt%) and a crystallinity of 40%. Note the step for 4 wt% due to the solubility limit at about 260 MPa. Uncertainty on DRE (grey) and corresponding compressible magma volume (pink) are based on the DRE estimation of ±50% (Wadge et al., 2014). The depth scale indicated assumes lithostatic pressure with a rock density of 2600 kg/m^3.

causes for the deformation pattern close to the volcano and modelled as a shallow deflating source could include cooling, crystallisation, outgassing and deposit loading. The most viable explanation for deep source volume changes is magma accumulation, whereas local and regional tectonics as well as crystallisation play a minor role, if any at all.

- We have tested the hypothesis that the inflation during pauses could be due the visco-elastic response of the volcanic system under constant pressure but without further magma influx. By utilising the linear deformation trend of a Maxwell rheology we found a set of parameters that could indeed explain the saw-tooth pattern for a simplified, homogeneous model (V_H). For more realistic, depth-dependent parameter distributions (VZ), however, we reject the hypothesis explaining the saw-tooth pattern without new magma influx. This is the case for all visco-elastic models we used despite stretching the parameter space concerning temperature and viscosity as far as possible.
- Our modelling has shown that the deformation data captured by the GPS network are controlled by the upper surface of the source volume and extending the source vertically, whilst maintaining its footprint, does not significantly alter the horizontal or vertical displacements. Hence, the absolute volume of the magma body to which volume changes are applied is hard to constrain and our preferred source geometry is not incompatible with previously published source volumes (summarised in Elsworth et al., 2014).
- By assuming a consistent source mechanism and geometry throughout the eruption, we have mapped the deformation field for all phases and pauses into volume changes at the deeper source, and conclusions can be drawn about magma supply and extrusion rates. We have calibrated our best-fit model parameters in Pause 5 and have applied those to the GPS data in previous phases and pauses. By retracing the entire eruptive history of SHV we have derived the total volume changes at the deep source level. Fig. 8 summarises and compares the volume of erupted material (DRE) and volume changes at depth based on the initial elastic models E_{1E}, while Table 3 contains the corresponding values derived from the volumetric strain integral for the depth-dependent, more realistic set of elastic and visco-elastic models VZ.
- Regarding the timing of the start of Phases 2–5, it is significant that the volume extruded has exceeded the volume of influx in each eruptive phase. This indicates that the magma reservoir has not been replenished to its original pre-eruption volume prior to the onset of the next eruptive phase. This fact demonstrates that the sequence of eruptive phases is not merely controlled by the accumulation of a critical magma volume, but another change in the system is required instigating an eruptive phase. Following this apparent trend of onsets indicated in Fig. 8 an intriguing interpretation could be made: the so-called ash-venting in the beginning of 2012 could be interpreted as a failed new eruptive phase.
- Another outcome of this study is the appreciation of how large the uncertainties in modelling parameters are, preventing the modelling results to be further constrained. This has been demonstrated in Elsworth et al. (2014) for purely elastic models and for visco-elastic models by Morales Rivera et al. (2019), as well as this study. Additional data sets like gravity measurements are needed to constrain the mass influx more directly.
- Currently there are three criteria which are used to define the end of the eruption at the Soufrière Hills volcano (Wadge and Aspinall, 2014). These are (i) absence of low frequency seismic swarms, (ii) daily SO_2 fluxes below 50 t/day, and (iii) no significant volcanic ground deformation from a deep source. Currently the latter two criteria are not being met. These two criteria are a proxy for continued input into the crustal magma storage system from depth of a hotter, volatile rich, more mafic magma. This input is thought to be necessary to sustain a long-lived, episodic eruption such as observed at the Soufrière Hills volcano. An exploration of the effects of a range of viscoelastic and elastic magma plumbing system models suggests that the observed ground deformation is best described by a continued pressurisation of a crustal reservoir thought to be due to input of mafic magma. As it is this input of mafic magma into the shallow storage system that is thought to have initiated and sustained the five extrusive phases of the Soufriere Hills Volcano (Devine et al., 2003), the implication is that another extrusive phase cannot be ruled out. We conclude that the eruptive sequence of Montserrat's Soufrière Hills volcano is still ongoing with magma trickling into a crustal reservoir. It remains an open question if there is enough crystal-poor, melt-rich, eruptible magma that could reach

the surface in the near future. To evaluate the near-term threat for Montserrat the crucial problem needs to be addressed why a new phase started in the past, when it started. Processes like segregation and turnover processes in a crustal reservoir of melt and crystal mush might hold the answer but are far from being understood. It also points to the need for continued close monitoring of the volcano to identify any signs of the beginning of a new phase of extrusion as early as possible.

Declaration of Competing Interest

The authors declare that they have no known competing financial interests or personal relationships that could have appeared to influence the work reported in this paper.

Acknowledgements

Thanks to the staff of the MVO who continuously monitor and assess the risk posed by the Soufrière Hills Volcano for access to the unique data explored in this study. We also thank them for contributions and insights shared during discussions with the Scientific Advisory Committee (SAC) which generated many of the ideas explored in this manuscript. We would like to acknowledge further contributions by SAC members Jenni Barclay, Eleonora Rivalta, and Fidel Costa, and thank Luca Caricchi for insightful discussions. The comments of two reviewers that improved the manuscript are highly appreciated. This research was supported by the Earth Observatory of Singapore via its funding from the National Research Foundation Singapore and the Singapore Ministry of Education under the Research Centres of Excellence initiative. This work comprises EOS contribution number 433. JN is partly funded by NERC Centre for the Observation and Modelling of Earthquakes, Volcanoes and Tectonics (COMET).

References

Caricchi, L., Simpson, G., 2015. Assessment of potential effect of degassing on the deformation observed at Soufriere Hills Montserrat since 1995. Appendix 10 in: 20th Report of the Scientific Advisory Committee on Montserrat Volcanic Activity. http://www.mvo.ms/.

Christopher, T.E., Blundy, J., Cashman, K., Cole, P., Edmonds, M., Smith, P.J., Sparks, R. S.J., Stinton, A., 2015. Crustal-scale degassing due to magma system destabilization and magma-gas decoupling at Soufrière Hills Volcano. Montserrat. Geochem. Geophy. Geosys. 16 (9), 2797–2811. https://doi.org/10.1002/2015GC005791.

Del Negro, C., Currenti, G., Scandura, D., 2009. Temperature-dependent viscoelastic modeling of ground deformation: applications to Etna volcano during the 1993-1997 inflation period. Phys. Earth Planet. Inter. 172 (3–4), 299–309. https://doi.org/10.1016/j.pepi.2008.10.019.

Devine, J.D., Rutherford, M.J., Norton, G.J., Young, S.R., 2003. Magma storage region processes inferred from geochemistry of Fe-Ti oxides in andesitic magma, Soufrière Hills volcano, Montserrat, WI. J. Petrol. 44, 1375–1400.

Dieterich, J.H., Decker, R.W., 1975. Finite element modelling of surface deformation associated with volcanism. J. Geophys. Res. Solid Earth 80, 4096–4102. https://doi.org/10.1029/JB080i029p04094.

Edmonds, M., Pyle, D.M., Oppenheimer, C., 2001. A model for degassing at Soufrière Hills Volcano, Montserrat, West Indies, based on geochemical data. Earth Planet. Sci. Lett. 186 (2), 159–173. https://doi.org/10.1016/s0012-821X(01)00242-4.

Edmonds, M., Pyle, D.M., Oppenheimer, C., 2002. HCl emissions at Soufrière Hills Volcano, Montserrat, West Indies, during a second phase of dome building: November 1999 to October 2000. Bull. Volcanol. 64 (1), 21–30. https://doi.org/10.1007/s00445-001-0175-0.

Edmonds, M., Humphreys, M.C.S., Hauri, E.H., Herd, R.A., Wadge, G., Rawson, H., Ledden, R., Plail, M., Barclay, J., Aiuppa, A., Christopher, T.E., Giudice, G., Guida, R., 2014. Pre-eruptive vapour and its role in controlling eruption style and longevity at Soufrière Hills Volcano. In: Wadge, G., Robertson, R.E.A., Voight, B. (Eds.), The Eruption of Soufrière Hills Volcano, Montserrat from 2000 to 2010. Mem. Geol. Soc. Lond, 39, pp. 291–315. https://doi.org/10.1144/M39.16.

Elsworth, D., Mattioli, G., Taron, J., Voight, B., Herd, R., 2008. Implications of magma transfer between multiple reservoirs on eruption cycling. Science 322 (5899), 246–248. https://doi.org/10.1126/science.1161297.

Elsworth, D., Foroozan, R., Taron, J., Mattioli, G.S., Voight, B., 2014. Geodetic imaging of magma migration at Soufrière Hills Volcano 1995 to 2008. In: Wadge, G., Robertson, R.E.A., Voight, B. (Eds.), The Eruption of Soufrière Hills Volcano, Montserrat from 2000 to 2010. Mem. Geol. Soc. Lond, 39, pp. 219–227. https://doi.org/10.1144/M39.12.

Feuillet, N., Leclerc, F., Tapponnier, P., Beauducel, F., Boudon, G., Le Friant, A., Deplus, C., Lebrun, J.-F., Nercessian, A., Saurel, J.-M., Clément, V., 2010. Active fault induced by slip partitioning in Montserrat and link with volcanic activity: New insights from the 2009 GWADASEIS marine cruise data. Geophys. Res. Lett. 37 (19), L00E15. https://doi.org/10.1029/2010GL042556.

Foroozan, R., Elsworth, D., Voight, B., Mattioli, G.S., 2010. Dual reservoir structure at Soufrière Hills Volcano inferred from continuous GPS observations and heterogeneous elastic modeling. Geophys. Res. Lett. 37 (19), L00E12. https://doi.org/10.1029/2010GL042511.

Foroozan, R., Elsworth, D., Voight, B., Mattioli, G.S., 2011. Magmatic-metering controls the stopping and restarting of eruptions. Geophys. Res. Lett. 38 (5), L05306. https://doi.org/10.1029/2010GL046591.

Gottsmann, J., Odbert, H., 2014. The effects of thermomechanical heterogeneities in island arc crust on time-dependent preeruptive stresses and the failure of an andesitic reservoir. J. Geophys. Res. Solid Earth 119, 4626–4639. https://doi.org/10.1002/2014JB011079.

Gudmundsson, A., 1990. Emplacement of dikes, sills and crustal magma chambers at divergent plate boundaries. Tectonophysics 176 (3–4), 257–275. https://doi.org/10.1016/0040-1951(90)90073-H.

Hautmann, S., Gottsmann, J., Sparks, R.S.J., Mattioli, G.S., Sacks, I.S., Strutt, M.H., 2010. Effect of mechanical heterogeneity in arc crust on volcano deformation with application to Soufrière Hills volcano, Montserrat, West Indies. J. Geophys. Res. Solid Earth 115 (B9). https://doi.org/10.1029/2009JB006909.

Hautmann, S., Witham, F., Christopher, T., Cole, P., Linde, A.T., Sacks, I.S., Sparks, R.S. J., 2014. Strain field analysis on Montserrat (W.I.) as tool for assessing permeable flow paths in the magmatic system of Soufrière Hills Volcano. Geochem. Geophys. Geosyst. 15, 676–690. https://doi.org/10.1002/2013GC005087.

Head, M., Hickey, J., Gottsmann, J., Fournier, N., 2019. The influence of viscoelastic crustal rheologies on volcanic ground deformation: insights from models of pressure and volume change. J. Geophys. Res. Solid Earth 124, 8127–8146. https://doi.org/10.1029/2019JB017832.

Herring, T.A., King, R.W., McClusky, S.C., 2010a. GAMIT: GPS Analysis at MIT Release 10.4, Internal Memorandum. Massachusetts Institute of Technology, Cambridge, MA.

Herring, T.A., King, R.W., McClusky, S.C., 2010b. GLOBK: Global Kalman Filter VLBI and GPS Analysis Program Release 10.4, Internal Memorandum. Massachusetts Institute of Technology, Cambridge, MA.

Hickey, J., Gottsmann, J., Nakamichi, H., Iguchi, M., 2016. Thermomechanical controls on magma supply and volcanic deformation: application to Aira caldera, Japan. Sci. Rep. 6 (1), 32691. https://doi.org/10.1038/srep32691.

Huppert, H.E., Woods, A.W., 2002. The role of volatiles in magma chamber dynamics. Nature 420, 493–495. https://doi.org/10.1038/nature01211.

Kokelaar, B.P., 2002. Setting, chronology and consequences of the eruption of Soufrière Hills Volcano, Montserrat (1995-1999). In: Druitt, T.H., Kokelaar, B.P. (Eds.), The Eruption of Soufrière Hills Volcano, Montserrat, from 1995 to 1999. Mem. Geol. Soc. Lond, 21, pp. 1–21. https://doi.org/10.1144/GSL.MEM.2002.021.01.02.

Le Mével, H., Gregg, P.M., Feigl, K.L., 2016. Magma injection into a long-lived reservoir to explain geodetically measured uplift: application to the 2007–2014 unrest episode at Laguna del Maule volcanic field, Chile. J. Geophys. Res. Solid Earth 121, 6092–6108. https://doi.org/10.1002/2016JB013066.

Lin, C.-Y., 2020. Alternative form of standard linear solid model for characterizing stress relaxation and creep: including a novel parameter for quantifying the ratio of fluids to solids of a viscoelastic solid. Front. Mater. 7, 11. https://doi.org/10.3389/fmats.2020.00011.

Lopez, A.M., Stein, S., Dixon, T., Sella, G., Calais, E., Jansma, P., Weber, J., LaFemina, P., 2006. Is there a northern Lesser Antilles forearc block? Geophys. Res. Lett. 33, 7. https://doi.org/10.1029/2005GL025293.

Manga, M., Hornbach, M.J., Le Friant, A., Ishizuka, O., Stroncik, N., Adachi, T., Aljahdali, M., Boudon, G., Breitkreuz, C., Fraass, A., Fujinawa, A., Hatfield, R., Jutzeler, M., Kataoka, K., Lafuerza, S., Maeno, F., Martinez-Colon, M., McCanta, M., Morgan, S., Palmer, M.R., Saito, T., Slagle, A., Stinton, A.J., Subramanyam, K.S.V., Tamura, Y., Talling, P.J., Villemant, B., Wall-Palmer, D., Wang, F., 2012. Heat flow in the Lesser Antilles island arc and adjacent back arc Grenada basin. Geochem. Geophys. Geosyst. 13, Q08007. https://doi.org/10.1029/2012GC004260.

Marsden, L.H., Neuberg, J.W., Thomas, M.E., 2019. Topography and Tilt at Volcanoes. Front. Earth Sci. 7 https://doi.org/10.3389/feart.2019.00317.

Mattioli, G.S., Herd, R.A., Strutt, M.H., Ryan, G., Widiwijayanti, C., Voight, B., 2010. Long term surface deformation of Soufrière Hills Volcano, Montserrat from GPS geodesy: Inferences from simple elastic inverse models. Geophys. Res. Lett. 37 (19), L00E13. https://doi.org/10.1029/2009GL042268.

McGee, L., Reagan, M., Handley, H., Turner, S., Sparks, R.S., Berlo, K., Barclay, J., Turner, M., 2019. Volatile behaviour in the 1995-2010 eruption of the Soufrière Hills Volcano, Montserrat recorded by U-series disequilibria in mafic enclaves and andesite host. Earth Planet. Sci. Lett. 524, 115730.

McTigue, D.F., 1987. Elastic stress and deformation near a finite spherical magma body: resolution of the point source paradox. J. Geophys. Res. 92 (B12), 12931–12940. https://doi.org/10.1029/JB092iB12p12931.

Mogi, K., 1958. Relations between the eruptions of various volcanoes and the deformation of the ground surfaces around them. B. Earthq. Res. I. Tokyo. 36, 99–134.

Morales Rivera, A.M., Amelung, F., Albino, F., Gregg, P.M., 2019. Impact of crustal rheology on temperature-dependent viscoelastic models of volcano deformation: application to Taal volcano, Philippines. J. Geophys. Res. Solid Earth 124, 978–994. https://doi.org/10.1029/2018JB016054.

Neuberg, J., O'Gorman, C., 2002. A model of the seismic wavefield in gas-charged magma: application to Soufrière Hills Volcano, Montserrat. Mem. Geol. Soc. Lond. 21, 603–609. https://doi.org/10.1144/GSL.MEM.2002.021.01.29.

Odbert, H., Taisne, B., Gottsmann, J., 2015. Deposit loading and its effect on co-eruptive volcano deformation. Earth Planet. Sci. Lett. 413, 186–196. https://doi.org/10.1016/j.epsl.2015.01.005.

Okada, Y., 1985. Surface deformation due to shear and tensile faults in a half-space. Bull. Seismol. Soc. Am. 75 (4), 1135–1154.

Okada, Y., 1992. Internal deformation due to shear and tensile faults in a half-space. Bull. Seismol. Soc. Am. 82 (2), 1018–1040.

Paulatto, M., 2011. Probing the interior of an active volcano: Three-dimensional seismic tomography at Montserrat, School of Ocean and Earth Science, University of Southampton, PhD thesis, p. 261.

Paulatto, M., Moorkamp, M., Hautmann, S., Hooft, E., Morgan, J.V., Sparks, R.S.J., 2019. Vertically extensive magma reservoir revealed from joint inversion and quantitative interpretation of seismic and gravity data. J. Geophys. Res. Solid Earth 124 (11). https://doi.org/10.1029/2019JB018476, 170–11,191.

Ryan, G.A., Shalev, E., 2014. Seismic velocity/temperature correlations and a possible new geothermometer: insights from exploration of a high-temperature geothermal system on Montserrat, West Indies. Energies 7, 6689–6720.

Segall, P., 2010. Earthquake and Volcano Deformation. Princeton University Press, Princeton, N.J, p. 213.

Segall, P., 2016. Repressurization following eruption from a magma chamber with a viscoelastic aureole. J. Geophys. Res. Solid Earth 121, 8501–8522. https://doi.org/10.1002/2016JB013597.

Stinton, A.J., Cole, P.D., Stewart, R.C., Odbert, H.M., Smith, P., 2014. The 11 February 2010 partial dome collapse at Soufrière Hills Volcano, Montserrat. In: Wadge, D., Robertson, R.E.A., Voight, B. (Eds.), The Eruption of Soufrière Hills Volcano, Montserrat from 2000 to 2010. Mem. Geol. Soc. Lond, 39, pp. 133–152. https://doi.org/10.1144/M39.7.

Stinton, A.J., Bass, V., Christopher, C., Fergus, M., Miller, V., Pascal, K., Rostant, D., Ryan, G.A., Stewart, R., Syers, R., Wade, V., Williams, P., 2020. MVO Open File Report OFR 20–01. Montserrat Volcano Observatory, Flemmings, Montserrat.

Voight, B., Widiwijayanti, C., Mattioli, G., Elsworth, D., Hidayat, D., Strutt, M., 2010. Magma-sponge hypothesis and stratovolcanoes: Case for a compressible reservoir and quasi-steady deep influx at Soufrière Hills Volcano, Montserrat. Geophys. Res. Lett. 37 (19) https://doi.org/10.1029/2009GL041732.

Wadge, G., Aspinall, W.P., 2014. A review of volcanic risk-assessment praxis at the Soufrière Hills volcano from 1997 to 2011. In: Wadge, D., Robertson, R.E.A., Voight, B. (Eds.), The Eruption of Soufrière Hills Volcano, Montserrat from 2000 to 2010. Mem. Geol. Soc. Lond., 39, pp. 1–40. https://doi.org/10.1144/M39.24.

Wadge, G., Herd, R., Ryan, G., Calder, E.S., Komorowski, J.-C., 2010. Lava production at Soufrière Hills Volcano, Montserrat: 1995–2009. Geophys. Res. Lett. 37 (19) https://doi.org/10.1029/2009GL041466. L00E03.

Wadge, G., Voight, B., Sparks, R.S.J., Cole, P.D., Loughlin, S.C., Robertson, R.E.A., 2014. An overview of the eruption of Soufrière Hills Volcano, Montserrat from 2000 to 2010. In: Wadge, D., Robertson, R.E.A., Voight, B. (Eds.), The Eruption of Soufrière Hills Volcano, Montserrat from 2000 to 2010. Mem. Geol. Soc. Lond., 39, pp. 1–40. https://doi.org/10.1144/M39.1.

Watts, R.B., Herd, R.A., Sparks, R.S.J., Young, S.R., 2002. Growth patterns and emplacement of the andesitic laval dome at Soufrière Hills Volcano, Montserrat. In: Druitt, T.H., Kokelaar, B.P. (Eds.), The Eruption of Soufrière Hills Volcano, Montserrat, from 1995 to 1999. Mem. Geol. Soc. Lond., 21, pp. 115–152. https://doi.org/10.1144/GSL.MEM.2002.021.01.06.

Yamasaki, T., Kobayashi, T., Wright, T.J., Fukahata, Y., 2017. Viscoelastic crustal deformation by magmatic intrusion: a case study in the Kutcharo caldera, eastern Hokkaido, Japan. J. Volcanol. Geotherm. Res. 349, 128–145. https://doi.org/10.1016/j.jvolgeores.2017.10.011.

Zellmer, G.F., Sparks, R.S., Hawksworth, C.J., Wiedenbeck, M., 2003. Magma emplacement and remobilization timescales beneath Montserrat: Insights from Sr and Ba profiles across plagioclase phenocrysts. J. Petrol. 44, 1413–1432.